ISOSPIN SYMMETRY IN NUCLEAR SCATTERING FROM ^{6}Li AND ^{12}C AT 280 MeV

by

Joseph Lloyd Mildenberger

B.Sc. University of Victoria 1984

M.Sc. University of Victoria 1987

A THESIS SUBMITTED IN PARTIAL FULFILLMENT OF

THE REQUIREMENTS FOR THE DEGREE OF

DOCTOR OF PHILOSOPHY

in the Department

of

PHYSICS

© JOSEPH LLOYD MILDENBERGER

SIMON FRASER UNIVERSITY

February 1990

APPROVAL

NAME: Joseph Lloyd Mildenberger

DEGREE: Doctor of Philosophy

TITLE OF THESIS: Isospin Symmetry in Nuclear Scattering from ^{6}Li and ^{12}C at 280 MeV

EXAMINING COMMITTEE:

Chairman: Professor E.D. Crozier

Professor O. F. Häusser
Senior Supervisor

Dr. K.P. Jackson
Senior Research Scientist, TRIUMF

Professor R.M. Woloshyn
Dept of Physics, SFU and TRIUMF

Dr. A.I. Yavin
External Examiner
Professor, School of Physics, Tel Aviv University

Date Approved: February 23, 1990

PARTIAL COPYRIGHT LICENSE

I hereby grant to Simon Fraser University the right to lend my thesis, project or extended essay (the title of which is shown below) to users of the Simon Fraser University Library, and to make partial or single copies only for such users or in response to a request from the library of any other university, or other educational institution, on its own behalf or for one of its users. I further agree that permission for multiple copying of this work for scholarly purposes may be granted by me or the Dean of Graduate Studies. It is understood that copying or publication of this work for financial gain shall not be allowed without my written permission.

Title of Thesis/Project/Extended Essay

Isospin Symmetry in Nuclear Scattering From ^{6}Li and ^{12}C at 280 MeV.

Author: _____
(signature)

Joseph Mildenberger
(name)

Mar. 24/90
(date)

Abstract

Tests of isospin symmetry in (n,p), (p,p′) and (p,n) reactions at 280 MeV for populating the $T = 1$ isospin triads in A=6 and A=12 nuclei have been performed at TRIUMF. DWIA calculations for the A=12 triad where the known ft asymmetry is included in the analysis show good agreement with experimental (n,p) and (p,p′) data. Similar calculations for the A=6 triad where no asymmetry was assumed show that twice the (p,p′) cross sections taken in the region q = 0.2–0.35 fm^{-1} are slightly ((5.1 ± 2.4)%) lower compared with the (p,n) and (n,p) cross sections at $\approx q = 0.1$ fm^{-1}. This asymmetry may be negligible when the data are extrapolated to $q = 0$. At $q = 0.67$ fm^{-1} the the (n,p) cross section is $\approx$ 45% larger than the (p,p′) cross section.

Dedication

In memory of my parents.

Acknowledgement

I would like to thank Prof. Häusser for taking me on as a graduate student and for financial support during this time, and for sharing with me his wealth of knowledge and experience in all stages of the experiment and analysis;and in particular for his assistance in the theoretical aspects of this work. As well, many people have assisted and advised me in many ways throughout the course of my work at TRIUMF: Mike Vetterli, Peter Jackson, Parker Alford, Ron Jeppesen, Anna Celler, Anne Trudel, Ken Hicks, Andy Miller, Robert Henderson, Stan Yen, Richard Helmer and Rudi Abegg.

To my fellow graduate students Bart Larson and Barry Pointon: your friendship was very special to me and will not be forgotten.

Finally, I must thank my wife Noni for her patience, support and understanding throughout all my years as a student. I could not have done it without you.

Contents

List of Figures

List of Tables

Chapter 1

Introduction

1.1 Isospin: A Brief History

The study of nuclear physics could be said to have begun with Rutherford's discovery (1911) that all of the positive charge and almost all of the mass of atoms was concentrated in a very small volume (the nucleus), with electrons forming a sort of planetary system around it. In this early model an atom with atomic number Z and mass number A was postulated to have a nucleus consisting of A protons and $A-Z$ electrons, with Z electrons orbiting around. Naturally, this model had grave conceptual difficulties due to the electrostatic repulsion of the protons which would cause the nucleus to break apart: some other "strong" force was needed in order to hold it together. This model also contradicted the experimental observation, revealed by the band spectrum of ^{14}N-^{14}N molecules, that ^{14}N obeys Bose-Einstein statistics. The discovery of the neutron by Chadwick (1932) led Heisenberg [1] to suggest just such a force, and also to introduce the concept of the "nucleon". However, he postulated the force as acting between neutrons and protons (n-p), but not between like particles (p-p or n-n).

This supposed property of the strong force evidently influenced Yukawa, whose meson theory of nuclear forces [2] (1935) originally included only charged π mesons.

Studies of the binding energies of ^{3}H and ^{3}He by Present [3] suggested the need for an n-n force, while "anomalous" behaviour observed in p-p scattering [4] was interpreted as being due to a strong p-p force. Breit *et al* [5,6] then postulated that it was reasonable to assume that all three of the nuclear interactions (n-p,n-n and p-p) were the same. In fact, this conclusion had already been reached the previous year by Young [7], who noted that the observed predominance of even N, odd Z nuclei demanded that "...strong attractive interactions exist between paired neutrons", and that "In order that the balance between protons and neutrons, within the nucleus, be preserved, similar forces must exist between paired protons". As well, the proportionality of the total binding energy with A, as opposed to Z, led him to suggest for the first time the complete charge independence[1] of the nuclear force.

The term "isospin" is a contraction of "isotopic spin", the label first proposed by Wigner in 1937 [8]. The name reflects the fact that the mathematics are exactly the same as are used for dealing with the spin angular momentum of particles, and that the z-projection of the vector, $\frac{1}{2}(N-Z)$, distinguished one isotope from another along an isobaric multiplet. Although by this time most of the pieces were in place, it was not until Kemmer [9] proposed the existence of a neutral meson, which would form an "isovector" triplet with its charged companions, that a potentially solid theoretical basis existed for the concept of charge-independence of the nuclear force.

The description of the proton and neutron as two different charge states of a single particle [1] was not a completely alien concept when it was first introduced; the mathematical formalism already existed in the form of the Pauli spin matrices,

[1]Discussions of isospin symmetry are generally categorized in terms of two different but closely related concepts, charge symmetry and charge independence. The principle of charge symmetry states that, in the absence of Coulombic interactions, the p-p and n-n forces are identical, while the stronger condition of charge independence would imply that all of p-p, n-n and n-p interactions are identical.

used to distinguish the two different states of spin-1/2 particles. And although Heisenberg's original formulation was simply a labelling device, he was quite correct in his supposition that the spin formalism was the correct way to deal with such a two-state system.

The subsequent expansion of Heisenberg's formulation to include like-particle forces as well as an n-p force (Wigner [8] asserted that the concept of isospin was "entirely useless" for charge-dependent forces) led to the understanding of many diverse nuclear phenomena in terms of isospin symmetry.

1.2 Tests of Isospin Symmetry

1.2.1 Nucleon-Nucleon Interactions

The charge-independence of nucleon-nucleon (NN) interactions would imply that the only differences between the neutron and the proton were electromagnetic in origin. At the time these concepts were evolving this was believed to be the case. It was generally held that, in principle, if all of the electromagnetic effects in NN interactions could be calculated and "subtracted", then we should find the hadronic n-p, n-n and p-p interactions to be identical. Over the years a very large effort has gone into both measurements of NN interactions and calculations of the various electromagnetic effects. Of course, both of these pursuits entail very significant problems: on the one hand the experimental quantities (particularly for n-n interactions) are very difficult to measure accurately; and on the other hand, the calculations of electromagnetic effects are model dependent, i.e. they depend particularly on the details of the short-range part of the hadronic force.

The most fundamental tests of charge symmetry and charge independence are measurements of NN scattering lengths (a_{NN}) and effective ranges (r_{NN}) in p-p, n-n

and n-p scattering at low energies. For projectile kinetic energies much less than ≈ 10 MeV, the scattering is almost entirely S-wave. The total cross section is

$$\sigma_s(E) = \frac{4\pi}{k^2} \sin^2 \delta, \tag{1.1}$$

where k is the wavenumber of the scattered particle and δ is the phase shift induced by the nuclear potential. Extrapolating the particle momentum to 0 we define

$$a \equiv \lim_{k \to 0}(-\frac{\sin \delta}{k}) \tag{1.2}$$

so that

$$\sigma_s(0) = 4\pi a^2 \tag{1.3}$$

As its name suggests, r_{NN} is a measure of how fast the potential falls off with distance, that is, it is a measure of the range of the nuclear force. The $^1S_0$ state is nearly bound; the scattering length has a large negative value, and significantly, small changes in the strength and width of the NN potential cause quite large changes in the scattering length ($\Delta a/a$), and somewhat smaller changes in the effective range ($\Delta r/r$) [10]. A recent summary [11] of the best available calculations and experimental results shows that there are indeed small but non-negligible charge-dependent (CD) and charge-symmetry-breaking (CSB) effects present in the $^1S_0$ NN state:

$$\Delta a_{CD} \equiv \frac{1}{2}(a_{nn} + a_{pp}^N) - a_{np} = 5.83 \pm 0.60 \text{ fm} \tag{1.4}$$

$$\Delta r_{CD} \equiv \frac{1}{2}(r_{nn} + r_{pp}^N) - r_{np} = 0.05 \pm 0.12 \text{ fm} \tag{1.5}$$

$$\Delta a_{CSB} \equiv a_{pp}^N - a_{nn} = 1.16 \pm 0.80 \text{ fm} \tag{1.6}$$

$$\Delta r_{CSB} \equiv r_{pp}^N - r_{nn} = 0.10 \pm 0.11 \text{ fm} \tag{1.7}$$

The N superscript denotes he extracted nuclear contribution after electromagnetic effects have been accounted for. These results imply that the difference in strength

between the n-n and p-p forces is $\approx 1\%$, while the n-p coupling is $\approx 2\%$ stronger than the average of the p-p and n-n strengths [12]. Theoretical calculations suggest that almost $1/2$ of Δa_{CD} can be accounted for by the mass difference of the charged and neutral π mesons [12].

These effects would be very troubling to our picture of nuclear forces if, as mentioned above, the neutron and proton were indeed identical apart from electromagnetic properties. But our current ideas concerning the structure of matter suggest a very plausible explanation for the observed asymmetry. It is now generally believed that the nucleons are not elementary particles, but are actually composed of more fundamental entities called quarks. In the "näive" quark model, the proton and neutron are both composed of three quarks, but in different combinations. While the proton has two "up" (u) quarks (each with charge $2/3e$, e being the charge of the electron) and one "down" (d, charge $-1/3e$), the neutron has one u and two d's. The u and d "flavors" do not have the same mass, as evidenced by the proton-neutron mass difference. So the "modern" picture is that on the most fundamental level, that is, in uu, dd and ud quark interactions, the hadronic forces are identical, but there is a breaking of symmetry due to the u-d mass difference. It is ultimately hoped that it will be possible to quantitatively explain all of the nucleon-nucleon symmetry-breaking effects by this mass difference. At the present time our ability to calculate nucleonic properties, much less NN interactions, is not advanced enough to be able to do this.

1.2.2 Isospin Symmetry in Nuclei

Since an isospin asymmetry is observed in NN scattering, we should not be surprised if we also find asymmetries in nuclei. It seems doubtful, due to our relatively imprecise knowledge of nuclear structure, that we can confidently identify the nu-

clear manifestations of the ≈1–2% effects observed in NN interactions, although some attempts have been made, as will be described below. When speaking of symmetry-breaking effects in nuclei we almost always are referring to the "conventional" phenomena such as electrostatic energy, magnetic effects and so forth. Thus, at least in the first approximation, the nuclear forces themselves are usually considered to be isospin invariant.

Strong evidence for charge symmetry can be seen in the masses and energy levels of mirror nuclei, i.e. pairs of nuclei with $N = Z \pm 1$ such as ^{3}H and ^{3}He, ^{7}Li and ^{7}Be, and ^{9}Be and ^{9}B. Once electrostatic energies are accounted for, the nuclei of a given pair have nearly the same mass, as well as showing very close similarities in their energy level schemes. The close correspondence of energy levels in even-A nuclei (such as the A=6 and A=12 triplets to be considered in this thesis) are arguments supporting the stronger condition of charge independence. But more detailed analyses [13,14] show that, as with NN scattering, careful calculations and subtractions of all known electromagnetic effects are unable to completely account for the measured mass differences between pairs of mirror nuclei (the so-called Nolen-Schiffer paradox). Attempts to relate these discrepancies to the more fundamental NN asymmetry (e.g. Ref. [13]) have met with mixed success. Of course, the calculations of electromagnetic effects in nuclei are even more complicated and model-dependent than for free nucleons.

In general, the symmetry-breaking effects in nuclei which we hope to measure and correctly identify with reasonable confidence are of the "conventional" (i.e. due predominantly to electrostatic effects) kind. Again, the most obvious systems to examine are isobaric multiplets.

Several effects may violate the isospin symmetry within a multiplet. For instance, isospin breaking is known to occur in β decay. The ft values for the

ground state decay of ^{12}B and ^{12}N provide a well-known example. The asymmetry, $\delta = ft^+/ft^- - 1 = 0.13 \pm 0.01$ [15], is consistent with the existence of a second-class induced-tensor weak current. However, a definitive experiment [16] which measured the excitation spectrum of ^{8}Be following the β-decays of ^{8}Li and ^{8}B showed that the strength of any second-class current was negligible and that δ in this case was almost certainly due to differences in the overlap of initial and final state wave functions caused by the weaker binding of the last proton compared with the last neutron. Blomqvist [17] subsequently showed that this effect was large enough to explain the A=12 ft asymmetry.

The A=12 ft asymmetry is actually very large. Studies of superallowed ($0^+ \rightarrow 0^+$) Fermi β decays, which are pure vector transitions, reveal that the ft values are very sensitive to small variations in the nuclear wavefunctions between different members of an isospin multiplet. Although model-dependent, calculations show [18] that differences in shell-model wavefunctions and radial overlaps are as small as 0.05% and 0.3%, respectively.

1.3 Isospin Symmetry in Nuclear Scattering

The measurement of transitions to members of an isospin multiplet from a common ground state is a very good method of testing isospin symmetry of the nuclear wave functions, as well as being a sensitive probe of the basic interaction which drives the transition. Cross sections for such transitions with $T_3^{\rm f} = 1, 0, -1$ are simply related by $\sigma_{p,n} = \sigma_{n,p} = 2\sigma_{p,p'}$, provided they have been corrected for Q-value effects and differences in distortions. The factor of two arises from the isospin coupling coefficients for the projectile. As well as the above-mentioned binding energy effects, isospin breaking effects can also be due to differences in distorted

waves for incoming and outgoing protons and neutrons; but since the transition densities are nearly the same for the final states in the multiplet one might expect this isospin breaking effect to be smaller than the overlap effects.

1.4 The Experiment and its Motivation

Although a more detailed description of the some of the theoretical aspects, particularly the techniques used to model nuclear reactions, will be given later on, it is necessary to introduce some of the basic principles and terminology now in order to discuss the aims and methods of the experiment.

1.4.1 The Nuclear Shell Model

While the discovery of the strong nuclear force answered a number of questions, a detailed and precise theoretical understanding continues to elude us. Even the simplest possible manifestation (NN scattering) cannot be completely described. The fact that the two-body interaction is not understood might lead one to conclude *a priori* that the many-body problem of nuclear structure is intractable. This is indeed true if what is desired is a description of nuclear properties in terms of meson exchange. But the problem has also been attacked in a more simplistic way which has had remarkable success. This is the "mean field" or "shell model" approximation. The essential assumption is that each of the nucleons in a nucleus moves in an average potential due to all of the other nucleons. The quantum-mechanical description of such a system leads to discrete states or "orbitals" for each nucleon. Since the nucleons are fermions (spin-1/2 particles) the Pauli exclusion principle limits he population of each orbital to one nucleon. Large energy gaps between particular sets of orbitals, differing in either principal or angular momentum quantum numbers, give rise to the "shell" structure. Nucleons are considered to be

either in the "core" (i.e. a filled shell) or in a "valence" state, that is an orbital in an unfilled shell. In the simplest models the central potential is all that is considered: the nucleons interact only with the mean (central) field. But more comprehensive models also include a spin-orbit interaction and a "residual" interaction between pairs of nucleons in the valence shell. The residual interaction between valence nucleons results in the mixing of states in the valence shell.

The core is usually considered to be "inert", that is, it does not take part in nuclear interactions with other particles. In most cases this is a good approximation because the energy difference between the highest-energy core orbital and the lowest-energy unfilled valence orbital is much greater than that required to excite a valence particle to another valence-shell orbital. This property greatly simplifies the theoretical modelling of nuclear reactions.

1.4.2 Modelling Nuclear Reactions

The two major ingredients needed in order to build a model of a nuclear reaction are nuclear structure and the dynamics of the interaction. The nuclear structure information is required to determine the transition densities between the initial and final nuclear states. The transition densities are a measure of the relative strengths of the transitions from particular components of the initial state to particular components of the final state, i.e. the transition densities depend on the coefficients of the "pure" shell model states which make up the initial and final nuclear states.

Nuclear structures can be determined by fitting single-particle energies and two-body matrix elements to empirically-measured binding energies and excitation energies for nuclei in the relevant mass region, in this case the 1p shell. The reliability of a nuclear structure calculation can be judged by how well the fitted matrix elements and single-particle energies reproduce the excitation energies and other

nuclear properties. This point will be discussed further in Chapter 4.

The calculations which have been used to model the reactions in this experiment use dynamical properties of the nuclear force deduced from experimental data. Specifically, the strengths and ranges of the various pieces of the nuclear interaction are determined from a phase-shift analysis of NN scattering data. This approach gives what is called an "effective interaction"; it merely describes the force rather than attempting to explain it from first principles. It is assumed that the valence nucleons behave essentially like free nucleons, except for kinematic considerations.

The reaction model used to combine the nuclear structure and the effective interaction to model nuclear reactions is called the Distorted Wave Impulse Approximation (DWIA). The major assumption of this model is that elastic scattering is by far the dominant process, and hence inelastic scattering can be treated as a perturbation. This is expressed in terms of an "optical potential" which contains both real (elastic) and imaginary (inelastic) pieces. The inelastic part reflects the *total* absorptive potential: no single inelastic process is considered to be dominant. The incident and final distorted waves are obtained by solving Schrödinger's equation for the optical potentials of the initial and final nuclear states, respectively. The optical potentials are derived by folding the effective interaction with experimentally determined matter distributions. This model assumes that the reaction is a single-step process i.e. impulse approximation.

1.4.3 Isovector Transitions in $A = 6$ and $A = 12$ Systems

The effective nuclear potential is actually a sum of several different types of interactions with different properties and selection rules. The various transition operators will be discussed in a later chapter. Of paramount importance to this work is one particular piece, the isovector $(\vec{\sigma}\vec{\tau})$ transition operator. Here, σ is the spin operator

and τ is the isospin operator. The $\vec{\sigma}\vec{\tau}$ operator changes the nuclear isospin quantum number T by one unit and changes T_z by -1, 0 and +1 for (p,n), (p,/ppr) and (n,p) reactions, respectively.[2]

The $\vec{\sigma}\vec{\tau}$ operator is the same operator as for Gamow-Teller (GT) β decay, whose angular momentum selection rules are:

$$\Delta J = 0, \pm 1 \text{ , no } 0 \rightarrow 0.$$

The fact that the same operator is responsible for these two very different processes would suggest that we might expect to find some sort of proportionality between β decay rates and cross sections of nuclear reactions which are mediated by the $\vec{\sigma}\vec{\tau}$ operator. In fact, this proportionality has indeed received much attention, both theoretically and experimentally. Such a relationship, if it could be reliably demonstrated, would enable the investigation of weak-decay processes into energetically-forbidden regions, as well as leading to a greater understanding of nuclear reaction mechanisms themselves [19].

A recent in-depth study of the relationship of (p,n) charge exchange cross sections at small angles to the corresponding β-decay transition states [19] found that for $L = 0$ spin-flip transitions in the DWIA model the cross-section could be expressed as

$$\sigma_{pn}(q,\omega,A,\alpha) = \hat{\sigma}^{-}_{GT}(A)F(q,\omega)B^{-}_{GT}(A,\alpha) \tag{1.8}$$

where q is the momentum transfer, ω is the energy loss and α specifies the final state of the recoil nucleus. $F(q,\omega)$ is a form factor, calculable in the DWIA model, which approaches unity as q and ω approach 0. Since $\hat{\sigma}^{-}_{GT}$ (referred to as the

[2]Nuclear physicists have traditionally defined $t_z = 1/2$ for the neutron, $-1/2$ for the proton. Particle physicists follow the opposite of this convention.

"unit cross-section") can also be calculated in the DWIA model, direct comparisons can be made between experimental measurements and theoretical predictions. An analogous relation exists for (n,p) reactions and β^+ decays.

The original motivation for this experiment was to provide an accurate determination of isospin violation for the Gamow-Teller (GT) matrix elements connecting the ^{6}Li (J^π=1^+,T=0) ground state with the J^π=0^+, T=1 isospin triad in ^{6}He, ^{6}Li and ^{6}Be. The forward-angle cross sections for the (n,p), (p,p′) and (p,n) reactions are proportional to the square of the matrix element of the $\sigma\tau_q$ operator ($q = -, 0, +$), with the proportionality constant determined by the ft value for the ^{6}He β^- decay. The GT ($\sigma\tau_0$) matrix element in ^{6}Li can then be compared to the M1 matrix element known from ^{6}Li(e,e′) experiments [20]. The M1 and GT matrix elements are dominated by identical spin parts but differ by meson exchange current (MEC) and orbital contributions, the latter being absent in the GT matrix element. Both the orbital and MEC effects can be reliably calculated in a light nucleus such as ^{6}Li [21,22], and any residual discrepancies between the axial vector and M1 matrix elements might then be ascribed to a change in the size of the nucleon inside the nucleus (an EMC-related effect). Such an interpretation is compatible with the "cloudy bag quark model" [23] in which the magnetic moment of the nucleon scales with the radius of the bag, while the axial vector coupling remains roughly constant. Calculations done for ^{12}C [21] have been used to deduce [24] an upper limit of 2% for a possible renormalization of the nucleon magnetic moment inside nuclei.

The $\vec{\sigma}\vec{\tau}_+$ matrix element determined from the accurately known β-decay rate of ^{6}He ($\log(ft) = 2.910 \pm 0.002$ (Ref. 25)) allows the proportionality constant determined from the (n,p) reaction to be used to calibrate the transformation of the

(p,p′) cross section to the matrix element of $\vec{\sigma}\vec{\tau}_0$:

$$\frac{d\sigma_{np}}{d\Omega}(q=0) = (\frac{\mu}{\pi\hbar^2})^2 \frac{k_i}{k_f} N_{\sigma\tau}^D |J_{\sigma\tau}|^2 B(GT^+) \tag{1.9}$$

$$B(GT^+) = \frac{1}{(2J_i+1)}[\langle J_f T_f | \Sigma\sigma\tau_+ | J_i T_i \rangle]^2 \tag{1.10}$$

$$B(GT^+) = \frac{1}{3}B(GT^-) = \frac{1}{3}(\frac{g_A}{g_V})^{-2}\frac{6163.4 \pm 3.8 sec}{ft} \tag{1.11}$$

In these expressions μ is the relativistic reduced energy divided by c^2, $N_{\sigma\tau}^D$ is a distortion factor representing the difference between PWIA (Plane Wave Impulse Approximation) and DWIA, k_i and k_f are wave numbers, $J_{\sigma\tau}$ is the volume integral of the $(\sigma\tau)$ component of the NN interaction, and $g_A/g_V = 1.261 \pm 0.008$ [25] is the ratio of axial vector to vector coupling constants. We do not make use of the factorized form of the cross section but employ instead the DW81 [26] code which also includes spin-orbit and tensor pieces of the NN interaction. For the pure GT transitions of interest, the latter account for $\leq 2\%$ of the cross section at 0°.

It is also necessary to measure the (p,n) cross section in order to determine possible isospin violation in the three matrix elements. As mentioned previously, such violations arise mainly from differences in the radial overlaps of the wavefunctions, which in turn can be attributed to differences in binding energies. The relation of the $\vec{\sigma}\vec{\tau}$ nuclear matrix elements to the GT β decay matrix elements implies that the magnitude of any observed asymmetry in 0° cross sections would be the same as the ft asymmetry. For this reason, transitions in the A=12 system were also studied. The A=12 system has been studied much more extensively than A=6; the cross section measurements and comparisons with theoretical calculations here can be used as a "control" of both the experimental and theoretical aspects of the A=6 system.

This somewhat ambitious program requires not only that the experimental quantities are measured with the highest possible precision, but also that the observed behaviours can be modelled and reproduced accurately.

In the experiment to be described, cross sections for (p,p'), (n,p) and (p,n) transitions to the lowest T=1 multiplets have been measured from the ^{12}C and ^{6}Li ground states. Simplified energy level schemes for $A = 12$ and $A = 6$ are shown in Fig. 1.1 and Fig. 1.2, respectively.

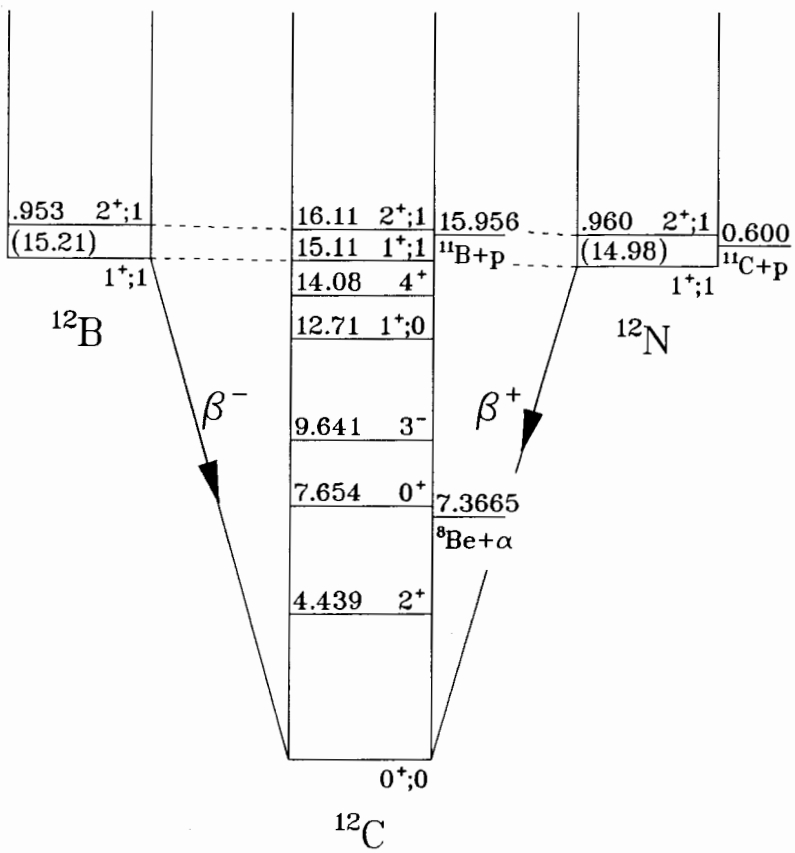

Figure 1.1: Energy level diagram for A=12. Data is from Ref. [15]. Dashed lines connect isobaric multiplets. The energies in brackets represent the (approximate) nuclear energies taken as $E_N = M(Z,A) - Z \times M(H) - N \times M(n) - E_C$, where M is the atomic mass excess in MeV and E_C is the Coulomb energy (taken as $E_C = 0.60Z(Z-1)/A^{1/3}$), minus the corresponding quantity for ^{12}C.

In both cases detailed theoretical calculations have been performed and compar-

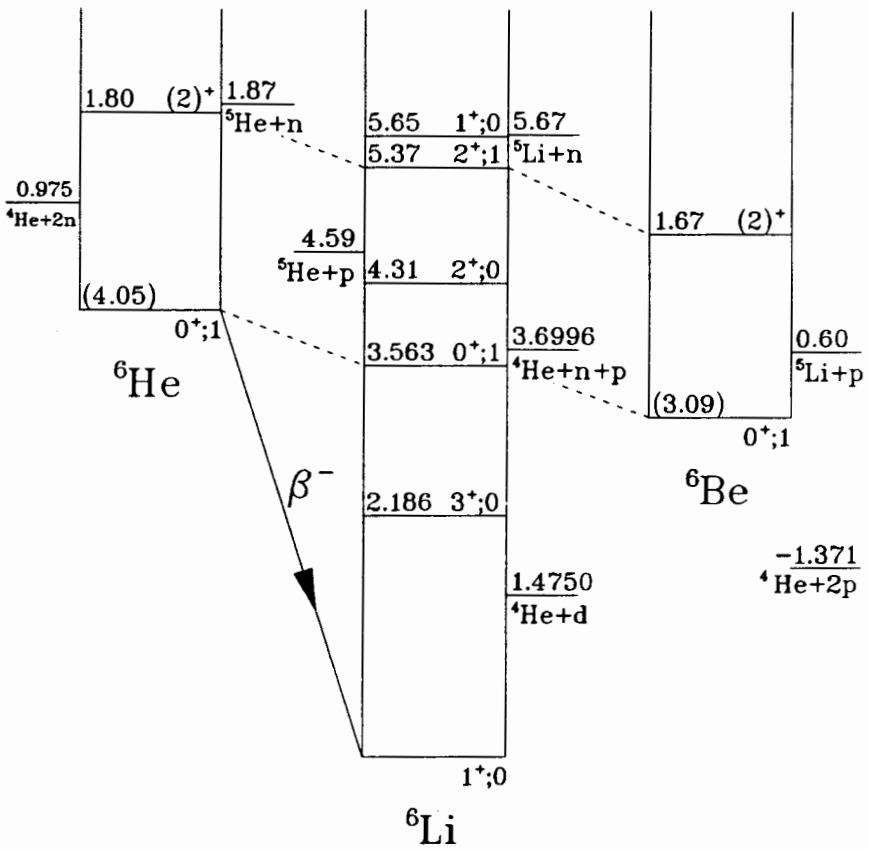

Figure 1.2: Energy level diagram for A=6. Data is from Ref. [27]. Dashed lines connect isobaric multiplets. The energies in brackets represent the (approximate) nuclear energies taken as $E_N = M(Z,A) - Z \times M(H) - N \times M(n) - E_C$, where M is the atomic mass excess in MeV and E_C is the Coulomb energy (taken as $E_C = 0.60Z(Z-1)/A^{1/3}$), minus the corresponding quantity for ^{6}Li.

isons made with the experimental data. A discussion of the peculiarities of these two systems will be left for a later section.

All three reactions proceed almost entirely by the relatively well-known $\vec{\sigma}\vec{\tau}$ component of the N-nucleus interaction. Since the dynamics of all three interactions are assumed to be the same, we have attempted to account for isospin symmetry violations in the two systems by using empirical structure parameters (where possible) in the theoretical descriptions of the interactions.

We must here acknowledge the serious difficulties, both experimental and theoretical, that are inherent in such an attempt to measure and explain nuclear structure effects on the several per cent level. Experimentally, we find that comparisons of cross sections for the three types of reactions are subject to significant uncertainties due to the differences in normalization procedures and systematic uncertainties in the measurements. For example, (p,n) cross sections are usually normalized to the "known" ^{7}Li(p,n)^{7}Be(g.s. + 429 keV first excited state) cross section at 0°, which is almost constant over a wide range of energies [28], but this cross section has an uncertainty of $\approx$ 10% [29,19]; (n,p) measurements are usually normalized to the (n,p) phase-shift solution of Arndt and Roper [30]. Absolute (p,p′) measurements at these energies are (in principle) straightforward but are subject to significant systematic uncertainties, as will be explained later. Theoretically, we find that while standard nuclear structure calculations of p-shell nuclei [31] do quite well for mid-shell nuclei such as ^{12}C, they disagree very significantly for masses 6–8. The reason for this is the rather pronounced cluster structure of these light nuclei, and the low two-particle emission thresholds (see Fig. 1.2). This in turn reduces the reliability of our DWIA calculations used to model the reactions. Other difficulties with the theoretical calculations will be discussed in a later chapter.

The experimental apparatus and techniques will be discussed in Chapter 2.

Chapter 3 will be mainly devoted to the data analysis, while Chapter 4 will describe in detail the theoretical calculations and comparison with the experimental results, including a discussion of sources of experimental uncertainty. A brief summary and conclusions will be given in Chapter 5.

Chapter 2

Experimental Method

The TRIUMF cyclotron accelerates H^- ions to energies continuously variable from 183 to 520 MeV. Beams are extracted by inserting into the beam a foil which strips both electrons from the ion. The magnetic field in the cyclotron causes the protons' trajectories to bend in the opposite direction from those of the H^- ions. The energy of the extracted beam can be changed by simply changing the radial distance of the extraction foil from the center of the cyclotron. The extracted beams are not monoenergetic; momentum spreads of $\Delta p/p = 0.15\%$ are typical. This corresponds to an energy spread of $\Delta E = 0.743$ MeV at $E = 280$ MeV. The extracted proton beam is directed into an evacuated beam pipe, where it is steered and focused by a series of dipole and quadrupole magnets.

All measurements were done using the Medium Resolution Spectrometer (MRS). The MRS is a large acceptance ($\Delta p/p \approx 15\%$) quadrupole-dipole magnetic spectrometer located on beamline 4B (BL4B) in the Proton Hall at TRIUMF. The MRS has a vertical bend plane, a solid angle acceptance of ≈ 2.5 msr, with an intrinsic energy resolution of ≈ 100 keV. More detailed descriptions of the various MRS components are given elsewhere [32]. A schematic diagram showing the major components of BL4B and the MRS is shown in Fig. 2.1.

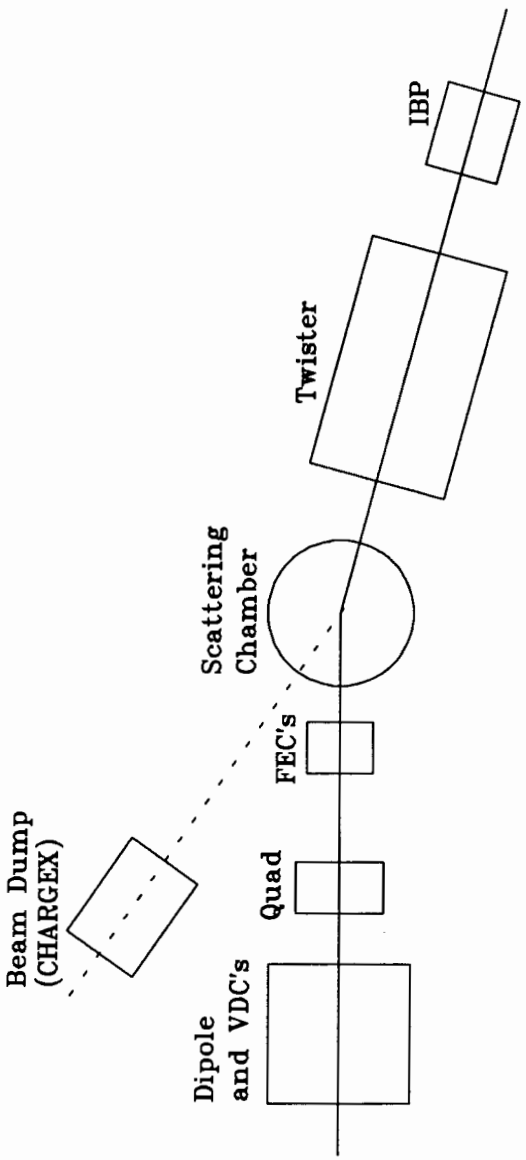

Figure 2.1: Schematic layout of main elements on beamline 4B (BL4B) in the proton hall at TRIUMF. The particular details of the FEC configuration and devices in and around the scattering chamber differ in (p,p′) and CHARGEX modes. This is shown in Fig. 2.2 and Fig. 2.3.

This experiment required the MRS to be arranged in two different configurations: small-angle (p,p′) (SAC) and charge-exchange (CHARGEX) modes. A more complete and detailed discussion of the CHARGEX facility can be found elsewhere [33]. Schematic diagrams of both configurations are shown in Fig. 2.2 and Fig. 2.3.

2.1 Small-angle (p,p′) Configuration

The small-angle (p,p′) configuration can be used to measure scattering from ≈3°–16°. The target is located at the MRS pivot, in an evacuated chamber continuous with the beampipe. A front-end chamber (labeled FEC0 in Fig. 2.2) located 107 cm downstream is ordinarily the first detector traversed by the scattered protons. The FEC is comprised of four wire planes, two each in the bend-plane (X) and non-bend plane (Y). The wire planes are labeled X_0, X_0', Y_0 and Y_0' with the primed planes being offset from the unprimed planes by one half of the anode wire spacing. Drift-time interpolation allows a spatial resolution of less than .5 mm (FWHM) to be achieved in each direction. The FEC performs two major functions:

- It enables ray-tracing of the proton's trajectory back to the target to allow software gates to be set (e.g. solid angle acceptance and target position), and is used for making corrections arising from aberrations to improve momentum resolution.

- A hit in one or both of the X and Y FEC planes is required in the MRS trigger under usual running conditions.

The principal component of the MRS detection system are two sets of vertical drift chambers (VDC's) separated by 39 cm and located at the top of the MRS (≈ 4 m beyond the exit of the dipole) near the focal plane. The VDC's are set at an

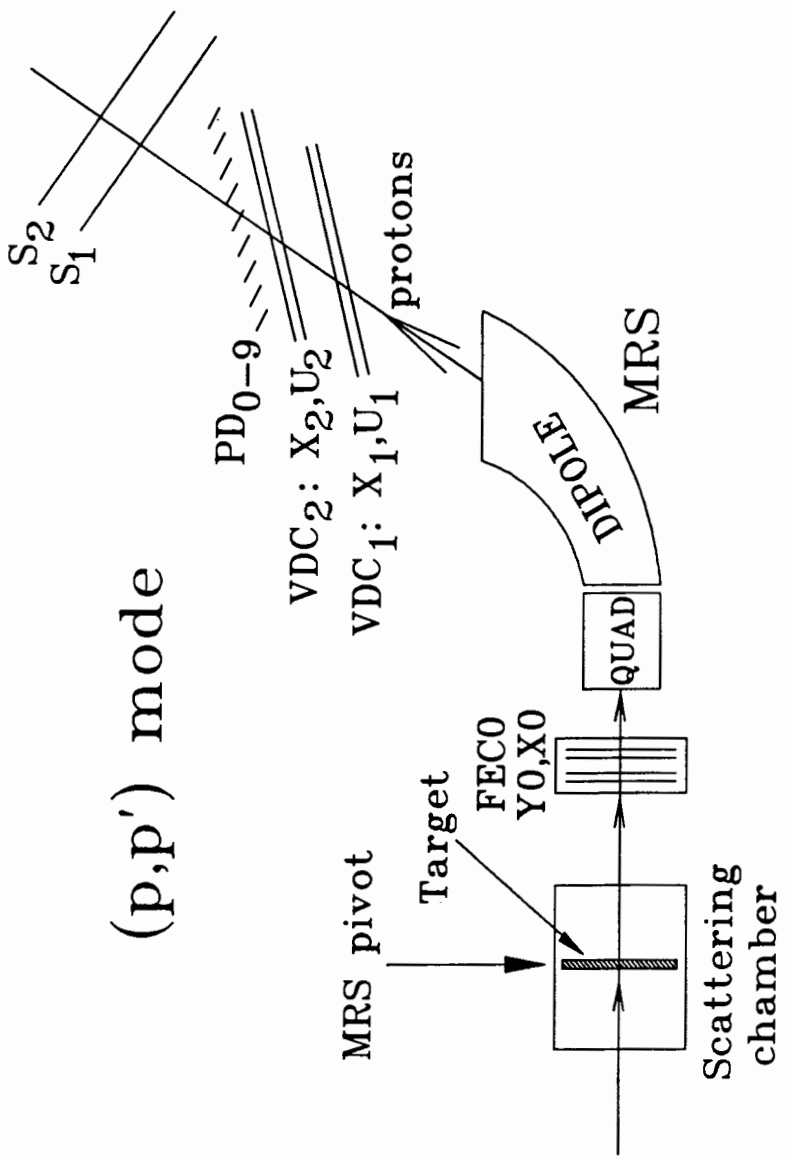

Figure 2.2: Schematic diagram of the TRIUMF Medium Resolution Spectrometer (MRS) in the (p,p′) configuration. See text for descriptions of the components.

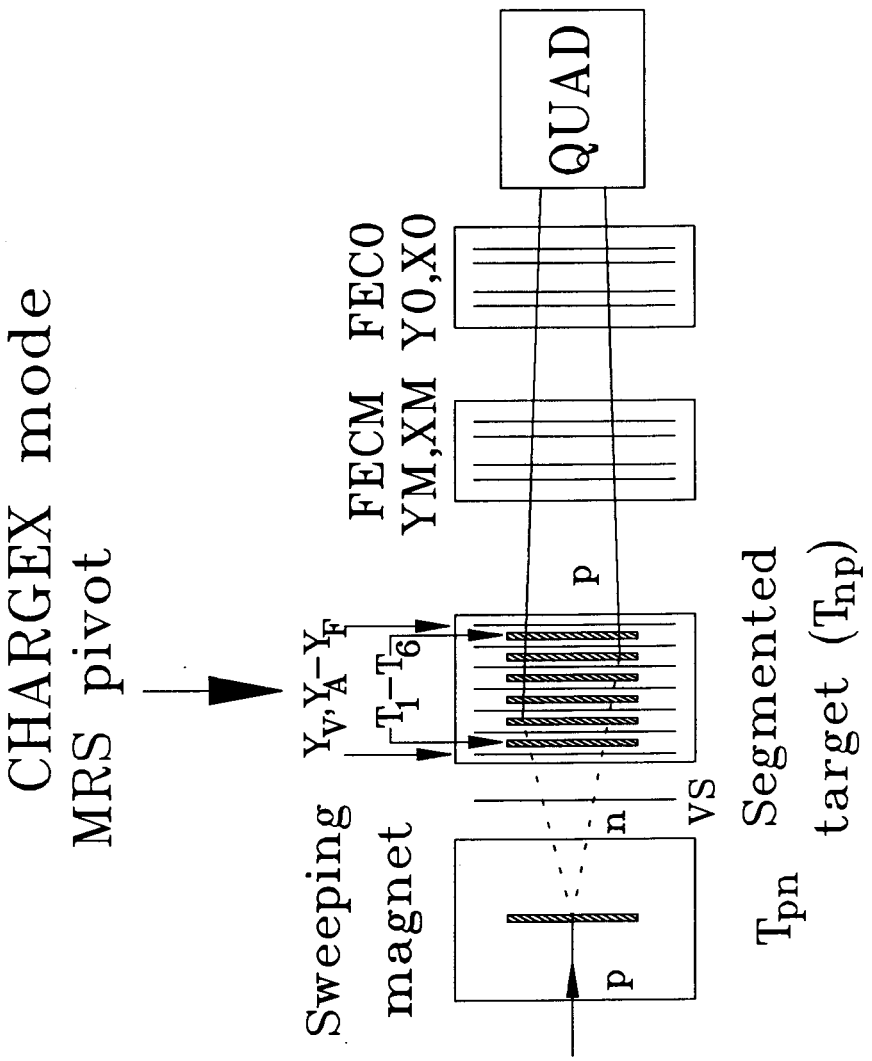

Figure 2.3: Schematic diagram of the TRIUMF Medium Resolution Spectrometer (MRS) in the Charge Exchange configuration. The rest of the MRS is the same as in Fig. 2.2. See text for descriptions of the components.

angle of 45° to the spectrometer exit axis with 2 planes each in the X (bend) and U (30° from x) directions, labelled X_1, U_1, X_2 and U_2 in Fig. 2.2. All four planes have a wire spacing of 6 mm; X_1 and U_1 each have 160 wires while X_2 and U_2 each have 176 wires. The position information from these planes is used to calculate the focal-plane position of the momentum-analysed protons. Located above the VDC's are 10 scintillators, labelled PD_0–PD_9. These are used to (roughly) select the range of momenta to be sampled by the data acquisition system, as well as being an important part of the event trigger (explained further in the next section). Two large scintillators, S_1 and S_2, cover most of the solid angle subtended by the focal plane, and can be optionally used in the trigger.

Optimum resolution is obtained in this configuration by using the technique of "dispersion-matching" which largely eliminates the beam energy-spread contribution. The beam is tuned such that it is dispersed horizontally in momentum; a six-quadrupole twister is used to rotate the momentum-dispersed beam by 90°. Thus, different beam momenta are vertically dispersed at the target by an amount so as to match the optics of the spectrometer. The trajectories of the high-momentum protons at the top of the target are bent less by the MRS dipole field than the low-momentum protons at the bottom; the proper dispersion matching condition causes all of the protons to hit at the same spot on the focal plane. Briefly, dispersion matching can be understood by considering a non-monoenergetic source of protons originating from a point on the focal plane, and traversing the MRS in reverse. On passing through the field of the dipole, the beam would be dispersed by an amount

$$\Delta X' = \frac{D_S}{M_S}\frac{(P'_H - P'_L)}{P'} \tag{2.1}$$

where D_S (M_S) is the dispersion (magnification) of the MRS, P'_H (P'_L) is the highest (lowest) momentum of the protons, and $P' = 1/2(P'_H + P'_L)$ is the average momentum. Thus for an incoming proton beam with spatial dispersion

$$\Delta X = D_T \frac{(P_H - P_L)}{P} \tag{2.2}$$

where D_T is the beam dispersion at the target, P_H (P_L) the highest (lowest) beam momentum, and the average momentum P defined as previously, the dispersion matching condition is obtained by simply setting $\Delta X = \Delta X'$. In practice an approximately correct beam tune is obtained from a beam transport program, and then fine-tuned by empirically adjusting the beamline and MRS magnets until the resolution is optimized.

Since no current integrating device is available in this configuration, beam normalization must be done indirectly using an in-beam polarimeter (IBP) [34], whose primary purpose is to monitor the polarization of the incident beam, upstream of the target position. Incoming protons scatter elastically off a thin polyethylene target into two pairs of counter telescopes located to the left and right sides of the beam axis, and each in coincidence with a recoil counter. The total number of scattered events, less the accidental coincidences, is proportional to the beam current. In order to calibrate the IBP, the MRS was changed to Large Angle Configuration, in which it is possible to run the beam into a Faraday cup. The Faraday cup was calibrated with a current source that had itself been calibrated with a factory-calibrated electrometer. Beam currents were typically .3 to .5 nA for this phase of the experiment. The combined uncertainties in the calibration are estimated to be $\leq .7\%$.

The ^{6}Li targets used in the experiment were fabricated on site. Since this material is very malleable it was possible to produce targets with uniform thickness

by using a small rolling mill and then cutting the targets to the desired size. The CH_2 targets were simply cut from sheets, while the ^{12}C targets were fabricated commercially in the form of graphite sheets.

Measurements of the chemical and isotopic purity of the CH_2 and ^6Li targets were performed: both the hydrogen abundance in the CH_2 (measured by gas chromatography) and the ^7Li contamination of the ^6Li (measured by nuclear magnetic resonance (NMR) analysis) were determined to $\leq .3\%$. The ^{12}C targets were actually natural carbon with a contamination of ^{13}C of 1.01%.

2.2 Charge-exchange Configuration

The same charge-exchange configuration was used for both the (n,p) and (p,n) measurements. In this mode (normally used only for (n,p) experiments) the primary target is located 92 cm upstream of the MRS pivot. For (n,p) running the $^7Li(p,n)^7Be$(g.s. and 429 keV) reaction is used to provide a nearly monoenergetic neutron beam. Neutrons emerging from this target proceed downstream to the secondary target located over the MRS pivot, while primary beam protons are deflected 20° by a sweeping magnet into a shielded beam dump. A small correction magnet upstream of the primary target is used to compensate for deviations in the primary beam trajectory caused by the fringe field of the clearing magnet. At the secondary target location is a segmented target box consisting of six target positions interleaved with eight vertical wire planes, the first two of which (labelled Y_v) act as a veto for any remaining charged particles. As well, a veto scintillator (VS) located immediately upstream of the target box is used to augment the wire-plane veto, and is also used in the trigger when the target box wire-plane efficiencies are measured (explained in more detail below).

A detailed description of the target box is given elsewhere [35]. Briefly, the operation is as follows. Neutrons produced in the primary target impinge upon the secondary targets in the target box. The proton emerging from an (n,p) charge-exchange reaction in one of the targets will be detected (assuming, for now, ideal efficiency) by all wire planes downstream of the target in which it converted. This allows an accurate calculation of the conversion location in all three dimensions. The protons from the (n,p) reaction are momentum-analyzed by the MRS exactly as in the (p,p′) configuration. One of the major advantages of the segmented target box is the capability to simultaneously take measurements for several different targets. This greatly reduces many potentially significant systematic uncertainties that could hamper the comparison of runs taken sequentially, e.g. beam integration, dead time and efficiency differences from run to run. The configuration of the six targets for the (n,p) part of this experiment, for target-of-interest X, was CH_2-X-X-X-X-CH_2(abbreviated by $CH_2(X)^4CH_2$). cross section measurements for targets X are taken relative to the H(n,p) cross section obtained from the SP88 phase-shift analysis [30]. For the (p,n) part of the experiment a stack of $(CH_2)^6$ was used. The background due to target gas and other material in the target box was measured by using a stack of $(empty)^5CH_2$.

The principal features of the segmented target box are that it can accommodate a large total target thickness without greatly compromising the resolution, and that accurate cross sections (relative to H(n,p)) can be obtained, because the measurements are done simultaneously with the H(n,p) measurement. In (p,n) running the target of interest is placed in the primary target position and CH_2 proton recoil targets are located in the target box. Since the primary target is not at the MRS pivot, only 0° measurements can be made with this geometry. In the charge-exchange configuration there are two sets of FEC's, labeled FECM and FEC0 in

Fig. 2.3. Position information from the two sets of FEC's is used to trace the trajectory back to the origin in the target box and compare it with the positions of the struck wires there. The hit co-ordinates on the struck target are used to define the "true scattering angle" by relating the extrapolated trace-back position vector to the vector whose endpoints are the center of the beam spot on the primary target and the hit location on the secondary target. Such a calculation is necessary both to enable corrections for kinematic effects due to different scattering angles, and, particularly in the (n,p) mode, to find the average scattering angle for a given MRS angle. This is a significant effect, as the reaction cross sections can vary rapidly with angle, even near 0°. When the MRS is set at 0° the average scattering angle for (n,p) reactions is $\approx 1.8°$. The target box wire-plane efficiencies are measured by inserting a thick piece ($\approx$ 1 cm) of CH_2 immediately upstream of the target box. Protons emerging from this converter pass through the veto scintillator and all the planes of the box, so that the number of "misses" for a given plane divided by the total number of protons passing through the box determines the efficiency of that plane. The observed efficiencies were of the order of 98–99%.

Beam normalization in CHARGEX mode was done directly with the beam dump used as a Faraday cup at the end of the beamline. Typical beam currents used for both the (n,p) and (p,n) measurements were 250 nA. Absolute beam normalization is not required in (n,p) running, as the cross sections are measured relative to the hydrogen (n,p) cross section, simultaneously with the (n,p) target of interest. In (p,n) running the relative integrated charge is required for run-to run comparisons. Leakage currents from the Faraday cup were measured periodically by turning the beam off and reversing the polarity on the Faraday cup; the leakage was consistently < 1 nA.

2.3 Data Acquisition and Event Triggers

The most important criterium for the event trigger is to maximize the proportion of useful events written to tape. At the same time, it is also necessary to be able determine the effieciencies of the detectors, and the "live time" of the data acquisition system, that is, the proportion of the time that the acquisition system is available to process events. Following is a brief description of the data acquisition system and event triggers used in the different phases of this experiment.

The MRS data acquisition system allows software-selectable triggers through the use of programmable LeCroy CAMAC (Computer Automated Measurement And Control) modules. This programmable trigger enables various combinations (in the form of logical AND's and OR's) to be used, depending on the particular circumstances of the run. In general, any trigger selected can be expressed as an AND of the "front-end trigger" (FETRIG) and the "top end trigger" (TOPEND). The possible inputs to FETRIG include the FEC's, an optional front-end scintillator (in (p,p') mode), and a veto scintillator (in CHARGEX mode). The minimal TOPEND trigger is simply a signal from any one of the 10 trigger paddles (any continuous range of trigger paddles can be chosen). This can be augmented by requiring an additional combination of hits from VDC X_1 plane and the S_1 and S_2 scintillators. The combination of FETRIG and TOPEND give what is called a "master" trigger which is a necessary but not sufficient condition to cause the event to be written to tape. A signal from either of the slit veto (which defines the limits of the MRS aperture),or the dipole vessel veto (to reject events scattering off of the wall of the MRS vacuum vessel) will generate a "fast clear" pulse, i.e. the acquisition system will be cleared and reset without recording the event on tape. As well, there is an additional movable scintillator, the "elastic prescaler" which enables the system to

accept a specified fraction of events in a particular focal plane region. As the name suggests, this is primarily used to reduce the number of elastically-scattered proton events from being written to tape in (p,p′) mode; in many cases, these events comprise the overwhelming majority and so swamp the inelastic data, which is usually what is of interest.

The information read by the data acquisition system consists of drift times and wire numbers (of hit wires only) for the wire chambers; timing and energy information for the scintillators. The timing and energy signals are digitized by time-to-digital converters (TDC's) and analog-to-digital converters (ADC's), respectively. The ADC's and TDC's are read in a user-specified order by the data acquisition program. Although the TDC's and ADC's can simultaneously convert an event while the previous one is being read, they cannot themselves accept another pulse while the previous one is being converted; so a "busy" latch is set to inhibit further acquisition while conversion is in progress.

For data events of the type described above, the data is written to tape in the following format:

1. Header (3 words: event length, event type, sequence number).

2. Digital Coincidence Register, which tells if the event is a pulser event (described below), and termination code.

3. TDC readouts (followed by a termination code), including: Time-of-flight of proton through the MRS ("TTB"); RF timing signal from cyclotron; Slit veto; Dipole vessel veto; S_1 scintillator; S_2 scintillator; Elastic prescale scintillator; front-end veto scintillator; front-end trigger scintillator.

4. ADC readouts from slit veto, dipole veto, trigger paddles, front-end veto,

followed by termination code.

5. VDC Header word followed by wire numbers and drift times for all drift-chamber wires which time out. This portion of the data record is of variable length.

Hits in wire chambers and scintillators, as well as the pulses generated by the various logical combinations of hits, are also counted and recorded by scalers. The scalers are read and written to tape periodically; typically, every 5 seconds. These constitute a separate event type from the data events described above. The scalers and scaler rates are available for the on-line monitoring of the detection and acquisition system.

Measurements of the live time of the data acquisition system (electronics and computer combined) are made by generating pseudo-events with a pulser. A random signal generator is set in coincidence with the beam current monitor; the rate is set such that the number of pseudo-events generated constitutes (typically) 5–10% of the total trigger rate. The live time of the system is simply given by the fraction of pulser events that end up being written to tape.

2.3.1 (p,p′) Triggers

Several different triggers were used for the (p,p′) runs, depending on the angle, and other circumstances. The TOPEND trigger used in all cases was simply a hit registered on any of trigger paddles 1–4. Elastic prescaling was used, the prescaling factor depending on the angle: 1 of every 200 elastic events was selected at the smallest angle (4.14°central angle); 1 of every ten at the largest angle (11.33°).

At small angles (4.14°–7.74°) FETRIG required hits in both FEC's, because the beam halo causes a large amount of accidental hits. At larger angles this condition

was relaxed by only requiring a hit in one of the FEC's. In order to accurately measure the wire chamber efficiencies, required to obtain absolute cross sections, some runs were also taken using the front-end scintillator (FES) as the only element in FETRIG. The FES was placed inside the scattering chamber and covered the most of the solid angle subtended by the FEC's. The trigger condition implied that any proton traversing the FEC's within this solid angle had to have passed through the FES. This trigger condition was essential to measuring absolute cross sections. This will be discussed in more detail later on.

2.3.2 CHARGEX Triggers

High beam currents require that triggers in CHARGEX mode be quite restrictive. Multiply-scattered protons from the primary beam cause high wire chamber rates in both the FEC's and the VDC's. This in turn can lead to a large number of accidental triggers being written to tape.

The TOPEND trigger required, as well as a hit in one of the trigger paddles, hits in both S_1 and S_2, and a hit in VDC X_1, while FETRIG required hits in both FEC's and no signal from the veto scintillator. This trigger was used for all of the (n,p) and (p,n) runs.

Chapter 3

Data Analysis

Most of the steps used in analyzing the data were very similar for both the (p,p′) and CHARGEX data. Following are descriptions of the major elements in the data analysis and measurement of cross sections. Presented first are general procedures common to both data sets. Following are separate sections which detail items in the analysis that differed from one data set to the other.

3.1 The LISA Data Analysis Program

Off-line analysis of the data was done using the LISA[1] data analysis program. Events are read and processed one at a time. LISA first determines whether the event is a "type 1" (scaler) or "type 2" (data) event. Type 1 events simply update LISA's scaler registers. The first stage in the analysis of type 2 events is to decode the drift chamber wire numbers and drift times into position co-ordinates for the struck wires. This is performed by the DRIFT routine, which also records for each chamber any "missing" or "multiple" hits. Next, in a user-specified interface (called the INSERT routine) quantities such as angles, focal plane co-ordinates and target co-ordinates are calculated and corrections are applied to the co-ordinates. Next, a series of user-defined conditions, either simple or complex, are applied to the co-

[1] LISA is an acronym that makes sense only in German.

ordinates. A second user-specified routine can then perform further manipulations on some condition-dependent subset of the processed co-ordinates. Histograms (1 and 2 dimensional) are then filled depending on the conditions specified in their definitions.

3.2 Particle Identification

The energy deposited in a thin scintillator by a particle with charge Z, kinetic energy T and momentum P is proportional to $(ZT/P)^2$; the time of flight over a fixed distance (non-relativistic) is proportional to (P/T). By looking at a two dimensional plot of the energy deposited in the hit trigger paddle versus the time of flight through the MRS (taken as the time difference between the FETRIG signal and the trigger paddle signal) it is possible to cleanly distinguish between different particles (e.g. protons, deuterons, pions) and set a gate to accept only the particles of interest, in this case protons.

3.3 Calculation of Secondary Co-ordinates

As mentioned above, the INSERT routine receives as input the raw wire chamber hit co-ordinates from the DRIFT routine and from these calculates secondary co-ordinates such as focal plane positions and angles.

A schematic diagram of the VDC is shown in Fig. 3.1. The X and U co-ordinates must be transformed into X and Y co-ordinates. It can be easily shown that with the 30° rotation of U relative to X, we get

$$Y = \sqrt{3}X - U \tag{3.1}$$

In order to have $Y = 0$ in the center of the VDC's, we must add an offset given by

$$C = 2U_c - \sqrt{3}X_c \tag{3.2}$$

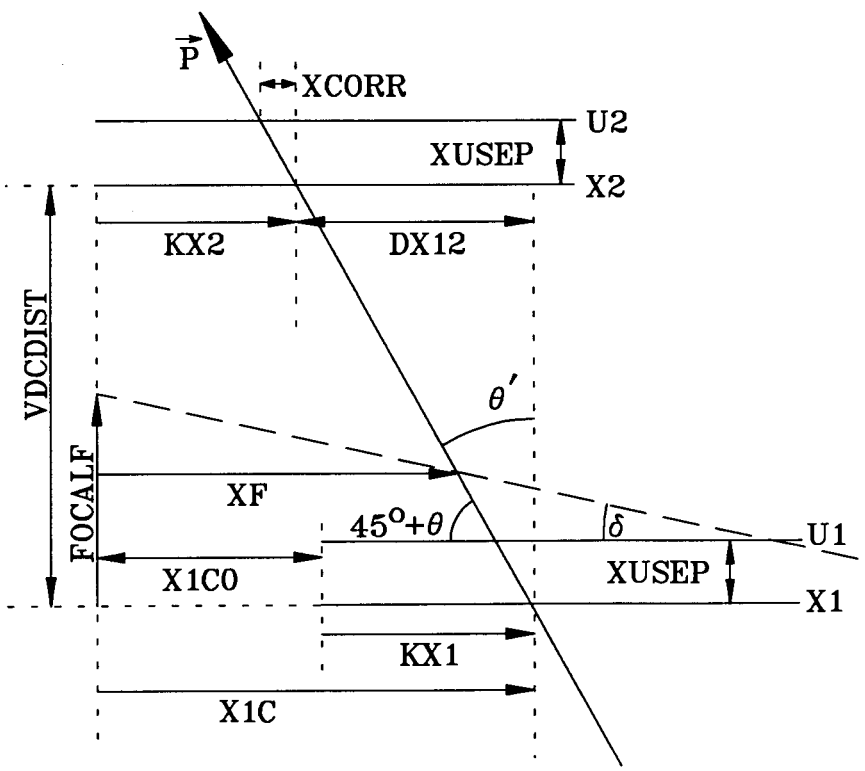

Figure 3.1: Geometry of VDC's and focal plane

where U_c (X_c) are the U (X) co-ordinates at the center of the VDC. For VDC1 $X_c = U_c = 8640$; for VDC2 $X_c = U_c = 10560$, using the standard 50 μm units of the MRS detector co-ordinates. These give offsets of 2315 and 2830 to Y_1 and Y_2, respectively. A further correction is necessary to take account of the distance between the X and U chambers. Examination of Fig. 3.1 shows that

$$XCORR = XUSEP(\frac{DX12}{VDCDIST}) \tag{3.3}$$

The fully-corrected Y is obtained by replacing X_1 (X_2) by $X_1 - XCORR$ ($X_2 - XCORR$). Although in principle this same technique could be used for both the (p,p′) and CHARGEX data, in practice it is used only in (p,p′) analysis. The non-bend co-ordinate is not necessary for any of the focal plane calculations, only for calculating the non-bend scattering angle and target co-ordinate. The extra set of FEC's in CHARGEX mode renders this information superfluous.

The calculation of the focal plane position, XF, is also straightforward. Consider a particle with trajectory $\vec{P}$ as shown in Fig. 3.1. The perpendicular distance (Z) from plane X1 to where the trajectory intercepts the focal plane is

$$Z_{\text{traj}} = \tan(45° + \theta)(X1C - XF) = \frac{VDCDIST}{DX12}(X1C - XF) \tag{3.4}$$

The focal plane is defined by

$$\tan\delta = \frac{(FOCALF - Z_{FP})}{XF} \tag{3.5}$$

where Z_{FP} is the distance from X1 to the focal plane. Setting $Z_{\text{traj}} = Z_{FP}$ we get

$$\frac{VDCDIST}{DX12}(X1C - XF) = FOCALF - XF \times \tan\delta \tag{3.6}$$

Solving for XF gives:

$$XF = \frac{(VDCDIST \times X1C) - (FOCALF \times DX12)}{VDCDIST - (DX12 \times \tan\delta)} \tag{3.7}$$

The bend-plane angle θ is calculated by taking the trigonometric identity

$$\tan(\theta_1 + \theta_2) = \frac{\tan\theta_1 + \tan\theta_2}{1 - \tan\theta_1 \tan\theta_2} \tag{3.8}$$

where $\tan(45° + \theta) = VDCDIST/DX12$, and making use of the small angle approximation $\tan\theta \approx \theta$ to get

$$\theta = 1000\frac{(VDCDIST/DX12) - 1}{(VDCDIST/DX12) + 1} \tag{3.9}$$

The angle θ is now in units of milliradians. In order to make the range of scattering angles independent of the momentum of the scattered protons, a momentum correction is applied to θ because the bend angle is greater (less) for particles of lower (higher) momentum. This is accomplished by applying a rotation in the XF-θ plane of the form

$$\theta_{pc} = \theta + TPXF \times (XF - XFTH) \tag{3.10}$$

The value of $XFTH$ is usually chosen such that θ_{pc} is centered at 0. The angle in the non-bend plane (ϕ) is simply

$$\phi = 1000\frac{Y_2 - Y_1}{\sqrt{(VDCDIST)^2 + (DX12)^2}} \tag{3.11}$$

where the small-angle approximation used previously has been applied. The units are again milliradians. As has been already mentioned, in CHARGEX mode ϕ is calculated from the FEC co-ordinates:

$$\phi_{\mathrm{FEC}} = 1000\frac{Y_0 - Y_m}{DFEC} \tag{3.12}$$

where $DFEC$ is the distance from FECM to FEC0.

The method used to obtain the target co-ordinates is different for (p,p′) and CHARGEX configurations. In CHARGEX mode the second set of FEC's makes

the trace-back to the target trivial, while a more complicated procedure is required in (p,p′) mode. In CHARGEX mode we have simply

$$Y_I = Y_M - \phi_{\mathrm{FEC}} \times FEC \tag{3.13}$$

$$X_I = X_M - \theta_{\mathrm{FEC}} \times FEC \tag{3.14}$$

Where FEC is the distance from the secondary target to FECM, and θ_{FEC} is defined analogously to ϕ_{FEC}. The distance FEC depends on which target the (n,p) conversion occurred in.

For (p,p′), in a manner analogous to the rotation in the XF-θ plane, we have

$$X_I = (X_0 + XITP \times \theta_{pc}) \times XIFC \tag{3.15}$$

$$Y_I = (Y_0 + FIFC \times \phi) \times YIFC \tag{3.16}$$

The parameters $XITP$ ($FIFC$) rotate X_I (Y_I) so as to be independent of θ_{pc} (ϕ); $XIFC$ and $YIFC$ are simply scale factors to reproduce the actual target size, and X_0 and Y_0 are the FEC hit co-ordinates.

A series of aberration corrections are applied to XF to optimize the resolution. As the focal-plane position is dependent on the target co-ordinates and scattering angles, it follows that the aberration corrections should be functions of these quantities. Typically, we might have

$$XFK = XF + a\theta_{pc}^2 + bX_I + c\theta_{pc}XI + d\phi_{FEC} \qquad \text{CHARGEX} \tag{3.17}$$

$$XFK = XF + a\theta_{pc}^2 + bX_I + cY_0 + dY_0^2 \qquad (\mathrm{p,p'}) \tag{3.18}$$

The Y_0 FEC measurement can be used in the second case because the small extension of the beam spot in (p,p′) configuration makes Y_0 directly proportional to ϕ. The correction coefficients can be obtained "by hand" by looking at 2-dimensional plots

of the particular variable *versus* XFK, or by using a computer program which minimizes the width of a particular peak in the XFK spectrum as a function of all the variables simultaneously.

3.4 MRS Efficiency

The overall MRS efficiency is simply the product of the individual efficiencies of all the wire chambers. The simplest method to obtain the individual efficiencies is to measure the probability that a given chamber will detect a particle that has also been detected by all of the other chambers. The efficiency for, say, VDC chamber X_1 is just the ratio of the condition counts

$$\epsilon_{X_1} = \frac{X_1 \times X_2 \times U_2 \times U_1 \times X_0 \times Y_0 \times PROT}{X_2 \times U_2 \times U_1 \times X_0 \times Y_0 \times PROT} \tag{3.19}$$

where the "×" implies a logical AND of hits in the specified chambers for each event. The condition $PROT$ ensures that the particle has been identified as a proton by the particle identification criterium described above. Analogous quantities are defined for the other chambers. The chamber efficiencies can vary depending on their counting rates; typical values for this experiment were 96–98% for the VDC's and 95–96% for the FEC's. Taking the overall MRS efficiency as simply the product of the wire chamber efficiencies tacitly implies that the trigger paddle efficiencies (and the FES efficiency for (p,p')) are identically unity. Although this is obviously not exactly true, their efficiencies are near enough to unity to make the difference negligible compared with the other uncertainties in efficiency.

3.5 Momentum Acceptance Correction

The MRS focal plane does not have a uniform acceptance for protons with different momenta, so it is necessary to determine the momentum acceptance function and

apply a correction factor to the measured number of counts in a given region in order to compensate. The technique is to vary the strength of the MRS dipole field, and measure the (yield/incident proton) in a particular peak (usually elastic scattering) as it moves across the focal plane. The counts in the peak are counted and normalized by the product of the integrated beam current, the MRS efficiency and the live time. A polynomial curve is then fitted to the relative acceptance as a function of focal plane position. The maximum value of the acceptance curve is set to be unity. Although the shape of the entire acceptance function is quite complicated, it can frequently be described by a quadratic function over the range of interest for a given experiment. This was indeed the case for both the (p,p′) and CHARGEX data from this experiment.

3.6 (p,p′) Analysis

3.6.1 Angle Calibration

The energy of protons scattered from a light nucleus falls more rapidly with increasing angle than those scattered from a heavier nucleus. Scattering from a CH_2 target is an ideal way to calibrate the MRS angle. At angles smaller than $\approx 7°$ (for $T_{beam} = 280$ MeV) protons from H(p,p) scattering have higher energy than those from the ^{12}C(p,p′)^{12}C(4.44 MeV) reaction, but lower energy at larger angles. Thus, a 2-dimensional plot of energy *v.* scattering angle (or equivalently, focal plane position *v.* Y_0) we can see where the "kinematic crossing" occurs as a function of the scattering angle. The value of Y_0 where the crossing occurs can be determined by eye from this plot, and compared with the calculated value of the crossing angle. A more accurate determination can be made, however. Plotted in Fig. 3.2 are the centroids of the focal plane positions of different Y_0 "slices" of the ^{12}C(4.44 MeV)

peak as a function of the central value of the Y_0 bin, at a (nominal) MRS central angle of 7.74°. In this case, the spectrum has been kinematically "tuned" for the

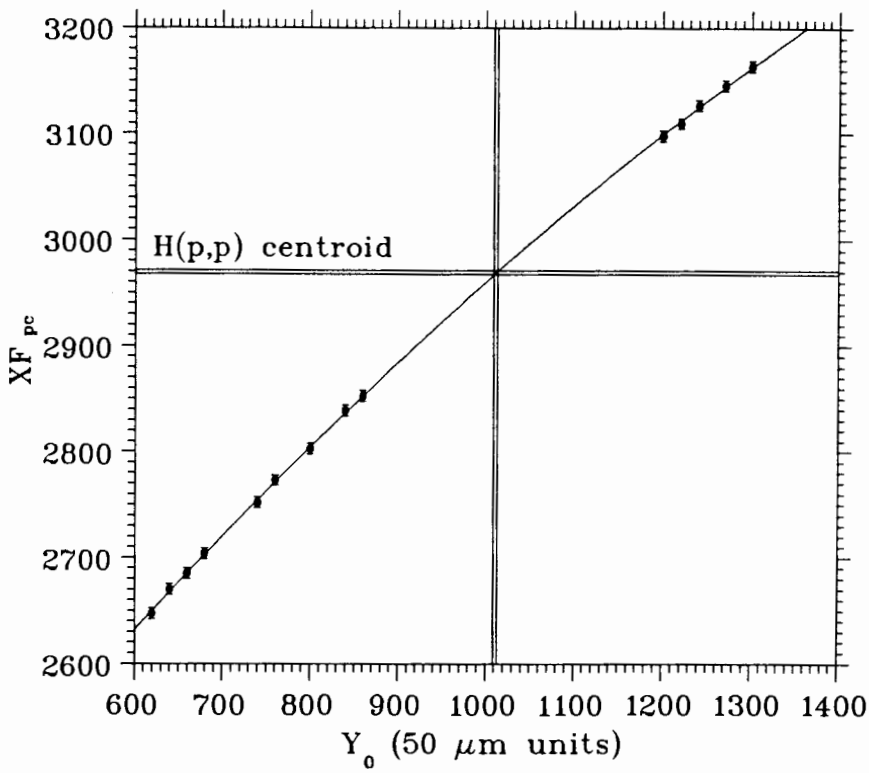

Figure 3.2: Kinematic crossing of H(p,p) and ^{12}C(4.44 MeV) peaks.

H(p,p) peak, i.e. the corrected focal plane co-ordinate $XFPC$ for this reaction is constant over the entire range of angles. The gap in the middle is where the ^{12}C peak is not resolvable from the H(p,p) peak. A quadratic function fitted to the centroid positions accurately shows the value of Y_0 where the kinematic crossing occurs. The center of the FEC is at channel 800; the crossing is at channel 1010 (in 50 μm units). As a first approximation it is assumed that the nominal angle is correct. The crossing angle is:

$$\theta_c = 7.74° - \frac{((Y_0)_c - 800) \times .005cm}{d_{FEC}} \times \frac{180}{\pi} \tag{3.20}$$

d_{FEC} is the distance from the target to the FEC's (107 cm). The above value of $(Y_0)_c$ gives $\theta_c = 7.18°$, compared with the calculated value of 7.06°. Thus, we must correct our nominal central angle by subtracting 0.11°.

3.6.2 (p,p′) Cross Section Measurements

The differential cross section for a scattering reaction can be defined as

$$\frac{\mathrm{d}\sigma}{\mathrm{d}\Omega} = \frac{N_{\mathrm{scat}}}{N_{\mathrm{inc}}} \frac{A}{N_0 \tau} \frac{1}{\Delta\Omega} \tag{3.21}$$

where A is the atomic weight of the scattering nucleus, N_0 is Avogadro's number, τ is the areal density of the target and $\Delta\Omega$ is the solid angle. The number of scattered particles is given by

$$N_{\mathrm{scat}} = \frac{N_{\mathrm{meas}}}{\epsilon(\mathrm{l.t.})(\mathrm{Acc})} \tag{3.22}$$

where ϵ is the total MRS efficiency, l.t. the combined electronics and computer live time, and Acc is the momentum acceptance function for the focal plane. The number of incident particles N_{inc} is obtained from the integrated beam current. The solid angle is calculated from cuts applied to the FEC co-ordinates X_0 and Y_0 and the target-FEC distance. The areal densities τ are corrected for known isotopic purities.

Absolute cross section were measured for the ^{12}C(p,p′)^{12}C(15.1 MeV;J$^\pi$=1$^+$,T = 1) and ^{6}Li(p,p′)^{6}Li(3.56 MeV;J$^\pi$=0$^+$,T = 1) transitions, and for H(p,p) elastic scattering. The targets used were ^{6}Li (41.0 mg/cm^2), CH_2 (44.5 mg/cm^2), ^{12}C(44.6 mg/cm^2) and a "laminated" target consisting of CH_2 and ^{6}Li targets of thicknesses 43.8 and 40.4 mg/cm^2, respectively. Measurements for all targets were made at (nominal) MRS central angles of θ_{MRS} = 4.14°,5.94°,7.74°and 9.54°.

Because the dispersed beam was wider than the targets, absolute beam normalization was done using the "achromatic" beam tune, focused to a small spot on the

target. This normalization was done at one angle only, 9.54°. For this run the FES (with assumed ideal efficiency) replaced the FEC's in the front-end trigger. Only one such measurement was necessary because the MRS angle settings overlapped sufficiently to allow a "bootstrapping" normalization technique from angle to angle, i.e. because the true yield per incident proton in the common angular region of adjacent MRS positions must be equal, normalization factors obtained from relating the measured yields for these regions were used to normalize the entire angular distribution of cross sections from one absolute measurement. The other major advantage was that the absolute current normalization, efficiencies and dead time were required only for the achromatic measurement at the one angle.

Absolute H(p,p) cross sections were obtained from the CH_2 target, after subtracting the carbon contribution, obtained from the ^{12}C target. For this procedure the ^{12}C data were analyzed with H(p,p) kinematic corrections. The ^{12}C spectrum was mormalized to the CH_2 spectrum by comparing the number of counts in a hydrogen-free region of the CH_2 spectrum with the same focal-plane region of the ^{12}C spectrum. For each MRS angle the data set was divided into three equal angular bins of 1.0°, except the 4.14° (central angle) data, for which the bins were 0.7° wide. No particular line shape was assumed; the H(p,p) peak areas were found by simple integration. The center of mass cross sections are given in Table 3.1.

As a test of the reliability of the absolute measurements, the data were compared with other H(p,p) data in the same energy region, and with the SP88 PP phase-shift solution of Arndt and Roper. Our data are in good agreement with a previous data set at 285 MeV [36] and are $\approx$ 7.5% below the SP88 PP phase-shift solution, as shown in Fig. 3.3.

Because it is unknown whether this difference stems from uncertainties in SP88 (there is very little experimental data near 280 MeV), or from systematic uncer-

$\theta_{c.m.}$ (deg.)	$d\sigma/d\Omega_{c.m.}$ (mb/sr)
8.29	4.42 ± 0.12
9.79	3.81 ± 0.10
10.43	3.70 ± 0.10
11.28	3.56 ± 0.09
12.61	3.49 ± 0.09
14.28	3.46 ± 0.09
14.79	3.40 ± 0.09
16.46	3.38 ± 0.09
18.17	3.42 ± 0.09
18.63	3.38 ± 0.09
20.35	3.39 ± 0.09
22.52	3.39 ± 0.09

Table 3.1: Absolute center of mass H(p,p) cross sections. The errors include statistical and systematic uncertainties.

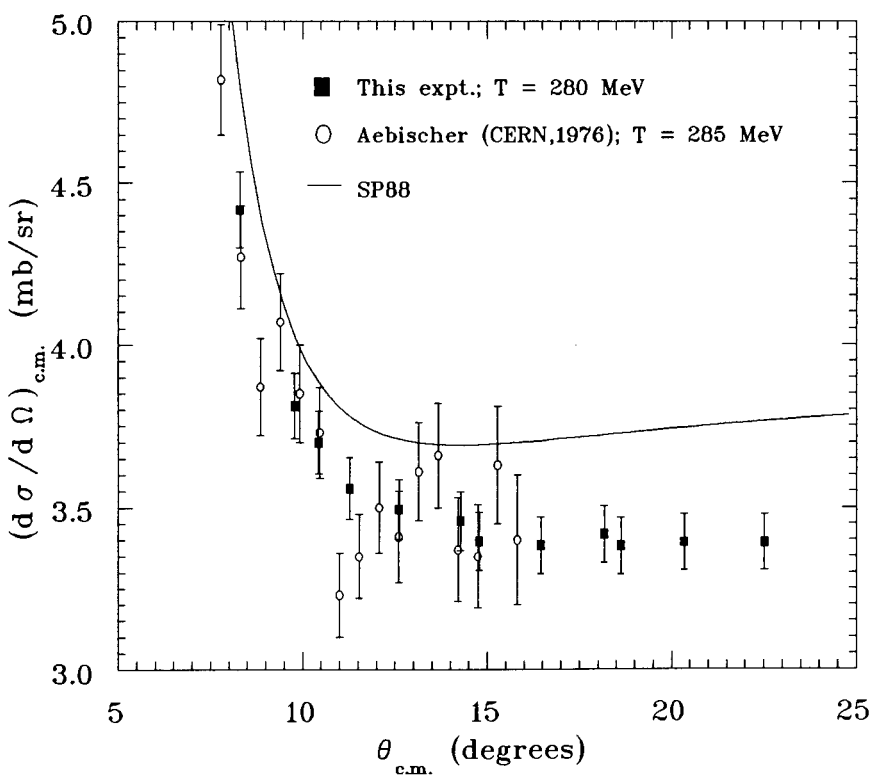

Figure 3.3: Absolute elastic (p,p) cross sections. The error bars for data from this experiment include both statistical and systematic uncertainties.

tainties in our measurement (i.e. uncertainties in the absolute value of the MRS momentum acceptance curve), we have normalized the (p,p′) data to agree with SP88. This has the added advantage of putting the (p,p′) data on an "equal footing" with the (n,p) data, because the (n,p) cross sections are normalized to the SP88 NP phase-shift solution. Also, the effective t-matrix used in N-nucleus interactions for the DWIA calculations [37,38] is based on the same phase-shift data. Thus, our assumption is that the SP88 NP and PP phase-shift solutions are correct *relative to each other*. The agreement between the ^{12}C(p,p′) and (n,p) data (presented in the next section) justify this assumption.

Cross sections for the ^{6}Li transition were obtained from two independent normalizations. The first involved using the laminated target combined with the absolute normalization obtained from the CH_2 target at 9.54°. A somewhat detailed, though straightforward series of comparisons was required to obtain the ^{6}Li(3.56 MeV) peak area from this technique. First, it was necessary to subtract the contribution of the ^{12}C in the CH_2 target in the region of the ^{6}Li peak. This was done by comparing the ^{12}C(15.1 MeV) peak of the single CH_2 target with its counterpart in the laminated target. The next step was to compare the ^{6}Li peak in the laminated target with the same peak in the single ^{6}Li target. All of this was done at 4.14°. The net result of this procedure was an overall normalization factor (which included efficiencies, dead time etc.) which applied to the single ^{6}Li target at that angle. Having achieved this, it only remained to use the above-mentioned "overlapping-angles" technique to get the ^{6}Li(3.56 MeV) cross sections at the other angles, using only the single ^{6}Li target. The second method was much more simple and direct. It used the achromatic-beam data from the single ^{6}Li target at 9.54° to directly calibrate the dispersed-beam data from the same target at the same angle. After that, the cross sections at the other angles were obtained as previously. These two normalization methods yielded cross

sections for the ^{6}Li(3.56 MeV) peak that agreed to $\approx$ .2%. This can be taken as an estimate in the run-to-run variation of beam-charge normalization, efficiencies and dead times. The very good agreement of these two methods of normalization also indicates that the target thicknesses were reliably measured.

The ^{12}C(15.1 MeV) peak cross sections were normalized by comparing the single ^{12}C target data with the ^{12}C from the CH_2 target at 9.56°. Again, the overlapping-angles method was used to get the cross sections at the other angles.

As with the H(p,p) data, none of the peak measurements assumed any particular lineshape. For both the ^{6}Li and ^{12}C measurements, there were non-negligible but smooth backgrounds; these backgrounds were fitted on either side of the peak with a polynomial function, and subtracted analytically from underneath the peak. Spectra for ^{12}C(p,p′) and ^{6}Li(p,p′) at θ_{lab}=4.1° are shown in Fig. 3.4 and Fig. 3.5, respectively.

3.7 CHARGEX Analysis

3.7.1 Corrections to (n,p) Spectra

Data from (n,p) reactions were obtained for ^{6}Li with the MRS at 0°, 3°, 6° and 10°; for ^{12}C at 0° and 3°; and at 0° only for the $(CH_2)^6$ stack. The previously mentioned effects due to the spread in scattering angles cause the average scattering angles to differ from the above values. The following corrections were applied to the data:

- Target box wire chamber efficiencies
- "Empty" (i.e. background) contributions from the target box
- "Leak-through" from upstream targets due to wire-plane inefficiencies
- Momentum acceptance of the MRS

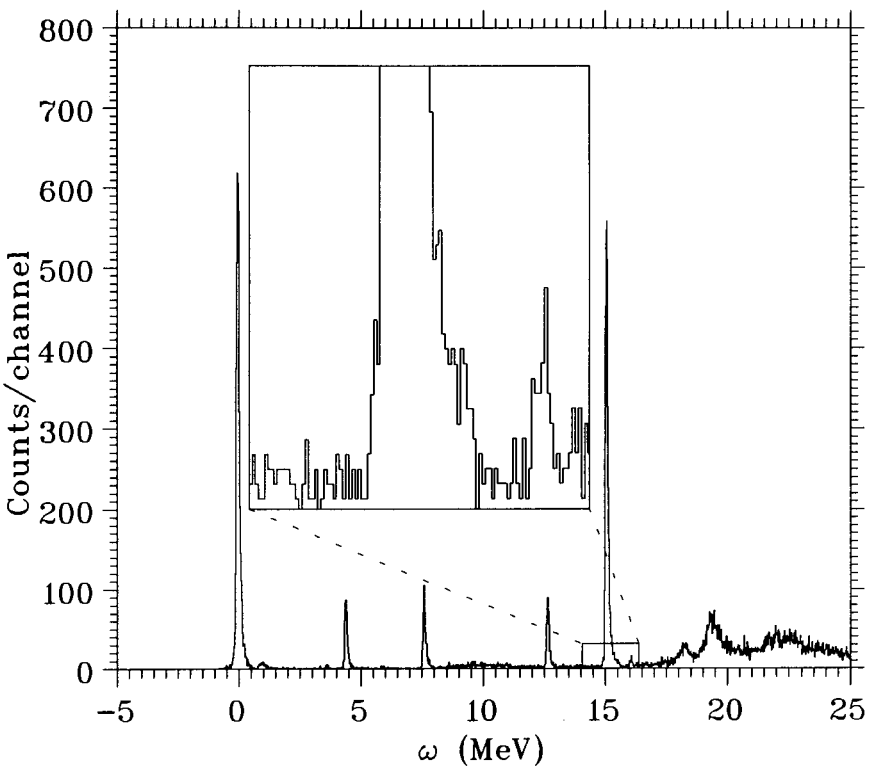

Figure 3.4: ^{12}C(p,p′) at θ_{lab}=4.1°. Spin, parity and isospin assignments for the states are given in Fig.1.1. The elastic peak has been scaled down by a factor of 200. The vertical scale in the inset runs from 0 to 30 counts.

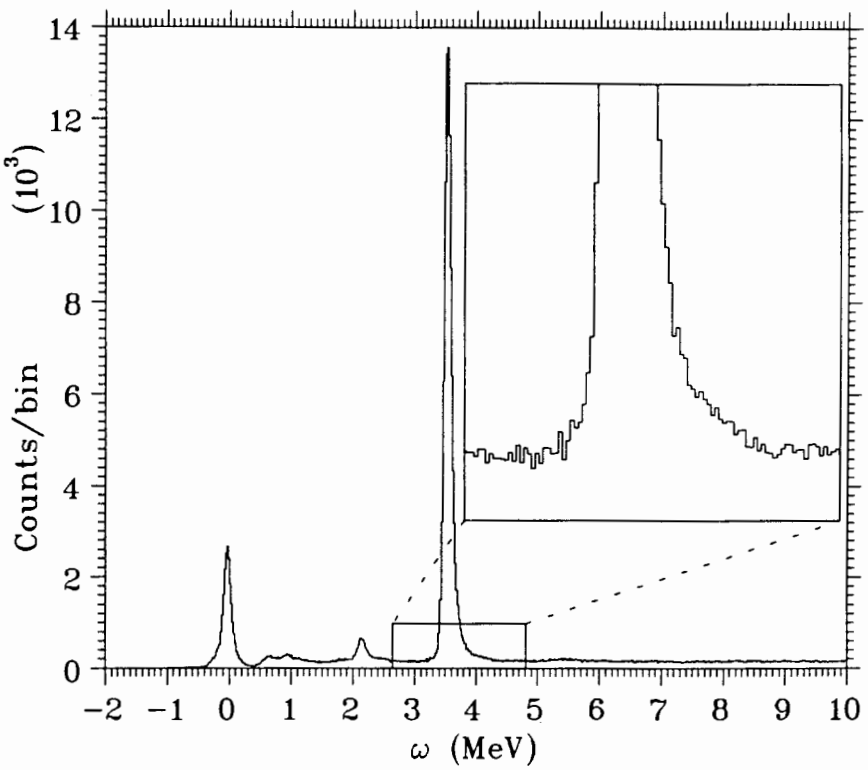

Figure 3.5: ^{6}Li(p,p′) at θ_{lab}=4.1°. Spin, parity and isospin assignments for the states are given in Fig. 1.2. The elastic peak has been scaled down by a factor of 200. The vertical scale in the inset runs from 0 to 100 counts.

- Low-energy neutron "tail" from the $^{7}Li(p,n)^{7}Be$ reaction

The method for obtaining the target box efficiencies was outlined in the previous chapter. The background contribution, due to (n,p) events in the detector gas and windows, was determined from data recorded with the (Empty)$^{5}CH_2$ stack. Before the empty spectrum obtained in this manner is subtracted from a given target spectrum it is shifted by an amount corresponding to the energy loss that would occur if the downstream targets had been in place. The magnitude of shift in any given instance is determined by the observed shifts of the given target spectum relative to the farthest downstream target. Because of the sparseness of the empty spectrum for any single plane (the contribution was typically $< 1\%$ of the target spectrum) the contributions from all of the planes were summed (with appropriate energy shifts) and an average empty spectrum was obtained which was used for all of the target subtractions. The empty spectrum was also "spread" to reflect the loss of resolution that occurs as the protons traverse downstream targets, although in practice this has virtually no effect on the corrected peak areas.

The "leak-through" correction is necessary because of the occasional misidentification of the target in which a given (n,p) conversion occurred. Consider a neutron converting in an upstream target for which the wire chamber immediately downstream did not fire, while all other downstream chambers did. This event would be (incorrectly) identified by the tracking program as having originated in the target immediately downstream from where it actually occurred. This effect was corrected by subtracting a fraction (determined by the efficiency of the chamber immediately upstream) of the spectrum from the target immediately upstream of a given target. Because of the high efficiencies of the wire planes, these corrections were typically on the order of $\approx 1\%$ or less.

The individual target spectra are corrected for these three effects (efficiencies, empty contribution, and leak-through) as follows. Let the individual wire chamber inefficiencies ($1-\epsilon$, where epsilon is the efficiency) be η_a, η_b, ..., η_f for wire planes Y_a, Y_b, ..., Y_f. The proton from a conversion in target a (upstream end) must be registered as a hit in all subsequent downstream planes Y_a–Y_f. The "cumulative efficiency" for plane Y_a is then the product of the efficiencies for all planes downstream, and similarly for the other planes:

$$\begin{aligned}
\alpha &\equiv (1-\eta_f)(1-\eta_e)(1-\eta_d)(1-\eta_c)(1-\eta_b)(1-\eta_a) \\
\beta &\equiv (1-\eta_f)(1-\eta_e)(1-\eta_d)(1-\eta_c)(1-\eta_b) \\
\gamma &\equiv (1-\eta_f)(1-\eta_e)(1-\eta_d)(1-\eta_c) \\
\delta &\equiv (1-\eta_f)(1-\eta_e)(1-\eta_d) \\
\epsilon &\equiv (1-\eta_f)(1-\eta_e) \\
\phi &\equiv (1-\eta_f)
\end{aligned} \tag{3.23}$$

If we assume that the combined inefficiency of the veto scintillator (immediately upstream of the target box) and the veto plane in the target box (Y_v) is negligible, and that the empty contribution is the same for all target positions, we can obtain explicit expressions for each target spectrum:

$$\begin{aligned}
A_m &= (A+e)\alpha \\
B_m &= (B+e+\eta_a A)\beta \\
C_m &= (C+e+\eta_b B)\gamma \\
D_m &= (D+e+\eta_c C)\delta \\
E_m &= (E+e+\eta_d D)\epsilon \\
F_m &= (F+e+\eta_e E)\phi
\end{aligned} \tag{3.24}$$

Here, A_m, ..., F_m are the measured spectra, A, ..., F are the "true" spectra and e is the empty spectrum. Starting with spectrum A and working down we can solve for the "true" spectra (neglecting terms of second order in η):

$$\begin{aligned}
A &= \tfrac{A_m}{\alpha} - e \\
B &= \tfrac{B_m}{\beta} - (1-\eta_a)e - \tfrac{\eta_a}{\alpha}A_m \\
C &= \tfrac{C_m}{\gamma} - (1-\eta_b)e - \tfrac{\eta_b}{\beta}B_m \\
D &= \tfrac{D_m}{\delta} - (1-\eta_c)e - \tfrac{\eta_c}{\gamma}C_m \\
E &= \tfrac{E_m}{\epsilon} - (1-\eta_d)e - \tfrac{\eta_d}{\delta}D_m \\
F &= \tfrac{F_m}{\phi} - (1-\eta_e)e - \tfrac{\eta_e}{\epsilon}E_m
\end{aligned} \tag{3.25}$$

Typical (n,p) and (p,n) spectra (after all corrections) are shown in Fig. 3.6 and Fig. 3.7, respectively.

3.7.2 (n,p) Cross Sections

As mentioned above, (n,p) cross sections are measured relative to the $^{1}H(n,p)$ cross section, obtained using CH_2 targets. Spectra from this reaction reveal a long, low-energy tail in the $^{7}Li(p,n)^{7}Be$ reaction which produces the neutrons. It is necessary to deconvolute the contribution due to this tail from the data. First, the contribution from the $^{12}C(n,p)^{12}B$ to the CH_2 spectrum is subtracted by comparing the CH_2 and $^{12}C(n,p)$ spectra. The remaining spectrum, shown in Fig. 3.8, represents the energy distribution of neutrons from the $^{7}Li(p,n)^{7}Be$ reaction. In practice the high-momentum (low bin number) end of the spectra is affected very little by the deconvolution: peak areas are typically reduced by $\leq 1\%$, thus introducing very little extra uncertainty into the cross section measurements.

The comparison of target yields from different locations in the box presents a number of difficulties. As well as having to take into account the wire plane efficiencies, there are also non-negligible differences in the neutron flux and solid angle subtended by the MRS. It was found that the target stacks used in this experiment eliminated the need to make explicit corrections for these effects. By making use of the relative yields of targets from the $(CH_2)^6$ stack (from (p,n) runs with ^{6}Li and ^{12}C primary targets, as well as the (n,p) runs with the ^{7}Li primary target) it was possible to map the relative yield as a function of target position. In this way it was found that the yield was a linear function of the target position. The yields varied on the average by $\approx 4\%$ over the length of the stack, with the maximum yields consistently at the upstream end. The statistical reliability of this procedure is demonstrated by the results shown in Fig. 3.9. The points represent

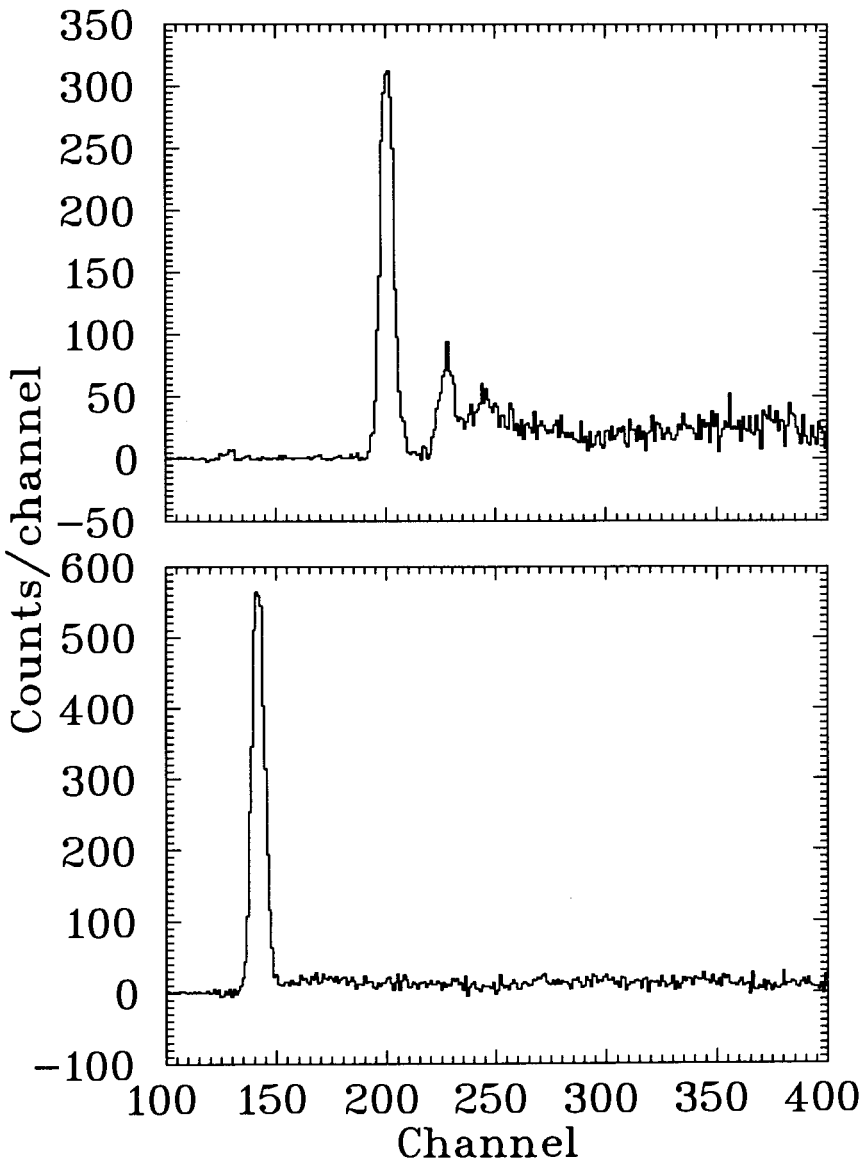

Figure 3.6: Typical (n,p) spectra (after all corrections) for ^{12}C (top) and ^{6}Li (bottom).

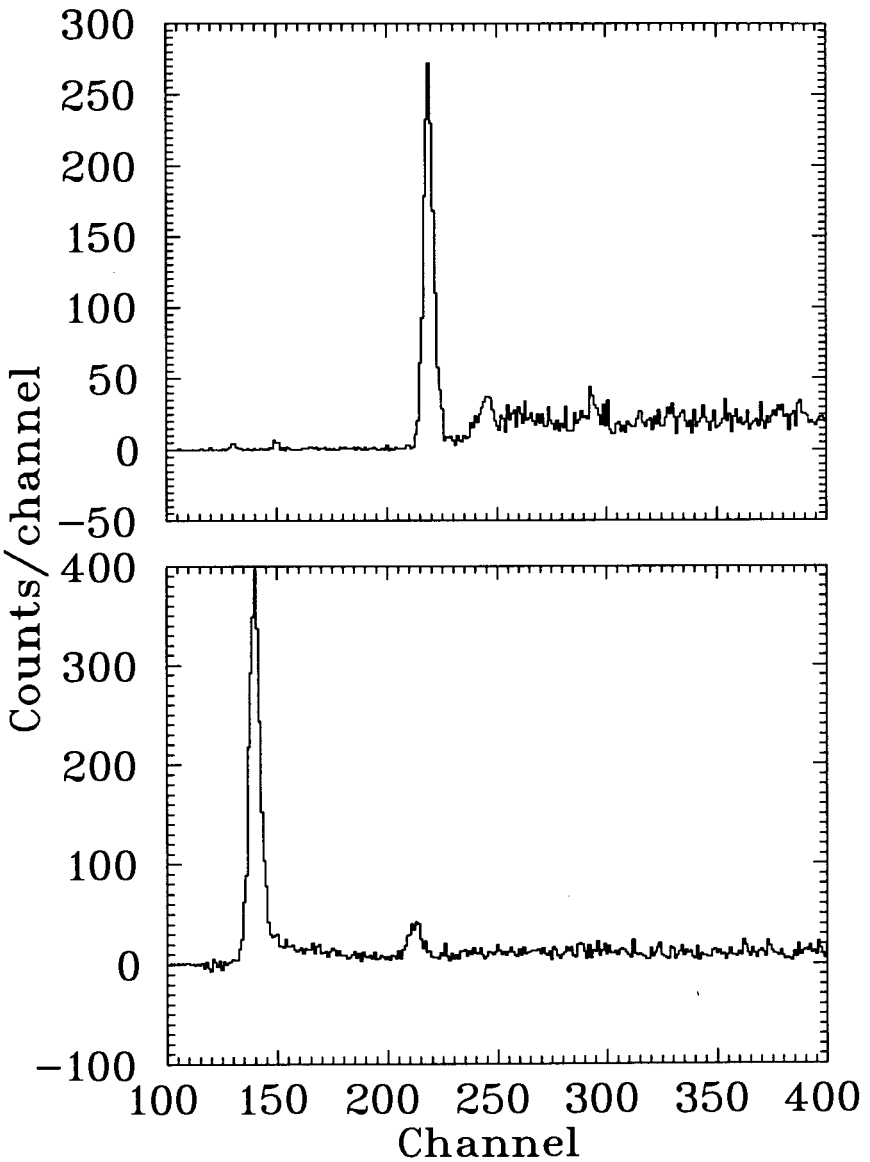

Figure 3.7: Typical (p,n) spectra (after all corrections) for ^{12}C (top) and ^{6}Li (bottom).

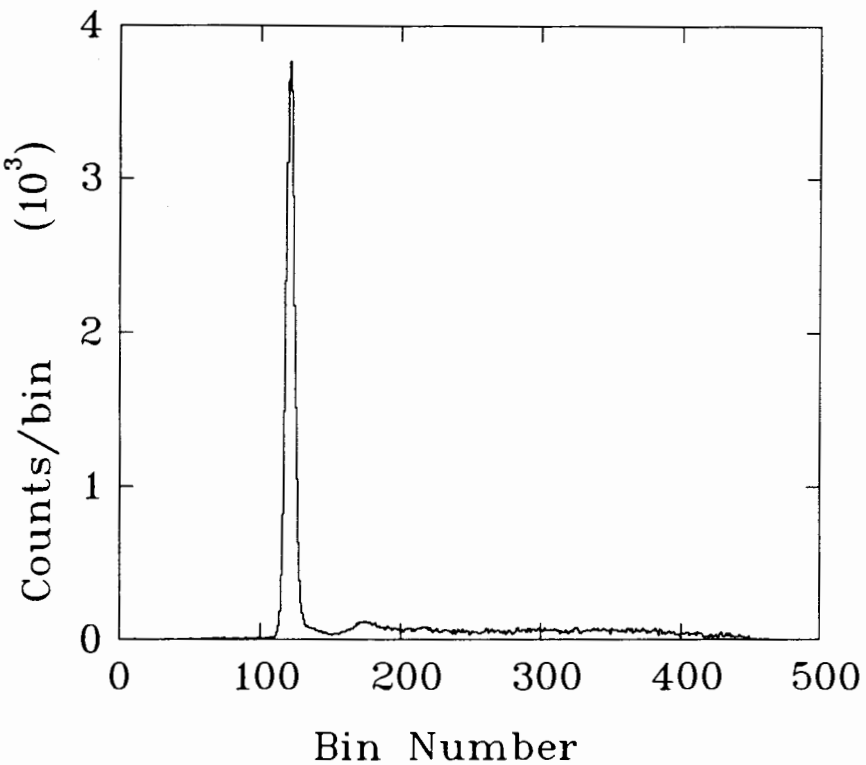

Figure 3.8: Neutron energy spectrum from the ^{7}Li(p,n)^{7}Be reaction

the relative (n,p) yields for all runs which employed the $(CH_2)^6$ target stack. The yields for each run are normalized such that the average yield is unity. The data represent measurements taken with five different primary targets: two ^{12}C targets, two ^6Li targets and one ^7Li target. A linear fit to the overall average for each target position also fits each of the individual data sets with $\chi^2 < 1$. This effect is due largely to the differences in the neutron flux between the upstream and downstream ends of the target stack. The relative (n,p) yields for ^6Li and ^{12}C were found by simply taking the average yield of the four ^6Li or ^{12}C targets divided by the average yield from the two CH_2 targets which bracketed them. The relative yield is simply

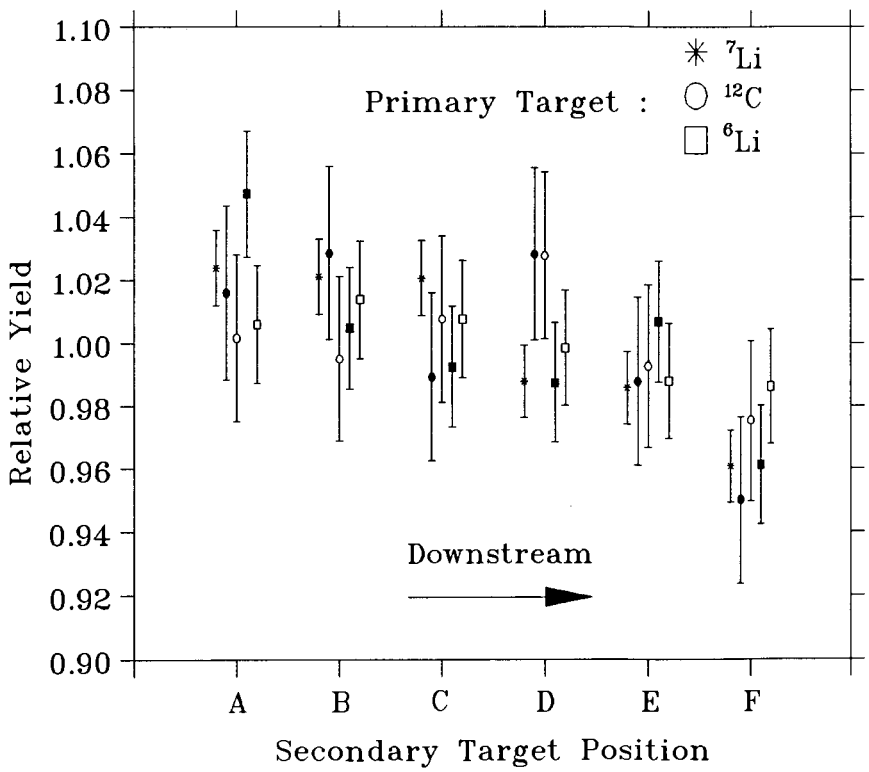

Figure 3.9: Relative (n,p) yields for segmented target box

the ratio of one cross section to another cross section.

As with the (p,p′) analysis, no particular line shape was assumed for the peaks of interest; as the subtractions and corrections outlined above virtually eliminated

the background (at least from the high-momentum end of the spectra) the peak areas were determined by simple integration of the peaks. Both the ^{6}Li and ^{12}C (n,p) spectra had weak non-zero regions on the low-momentum side of the peaks of interest, but as these were small compared with the peak area, no background was assumed under the peaks. However, the statistical uncertainties were in this case increased to take into account the difficulty in determining any possible background contribution.

3.7.3 (p,n) Cross Sections

As mentioned previously, (p,n) measurements were performed at 0° only. Since the (p,n) configuration was in this case identical to the (n,p) configuration most of the corrections applied were of a very similar nature, but two significant differences will be pointed out.

First, the target-empty correction is less significant than in the (n,p) case, because the ^{1}H(n,p) cross section at 0° ($\approx$ 54mb/sr) is several times greater than for either ^{6}Li or ^{12}C: $(\sigma/\sigma_{\mathrm{H}})_{0°;\mathrm{lab}} \approx .38$ for ^{6}Li; $\approx .18$ for ^{12}C. Furthermore, since comparisons must be made from run to run, the VDC and FEC efficiencies, dead time and beam current must be taken into account. It was assumed that the target box efficiencies remained the same for different runs. Two sets of runs, with different primary targets, were done for both ^{6}Li and ^{12}C. The measured yields were consistent to $\leq$ 1.8% for ^{6}Li, and to $\leq$ 1.2% for ^{12}C. This is taken to be an estimate of the variation for these measurements.

Peak areas for the ^{12}C(p,n) spectra were found by simple integration. A small background, due mainly to ^{13}C impurities, was taken into account by subtracting the counts over a region equal to the peak width immediately adjacent to the peak. This accounted for $\approx$ 2.5% of the entire peak area.

The ^{6}Li(p,n) line shape necessitated a somewhat more complicated procedure to obtain the peak area. Because of the unbound nature of the ^{6}Be ground state, the peak had a large low energy tail. To get an estimate of how much of the peak area was in this tail, the lineshape was compared with that from the ^{6}Li(n,p)^{6}He reaction. The number of counts in the high-momentum side of the (n,p) peak was normalized to the same region of the (p,n) peak. The reliability of this procedure can be seen in the agreement of the background heights and shapes on the low-momentum side of the curve, shown in Fig. 3.10. (The second peak in the (p,n) spectrum is simply the "echo" caused by the carbon in the CH_2 converters.)

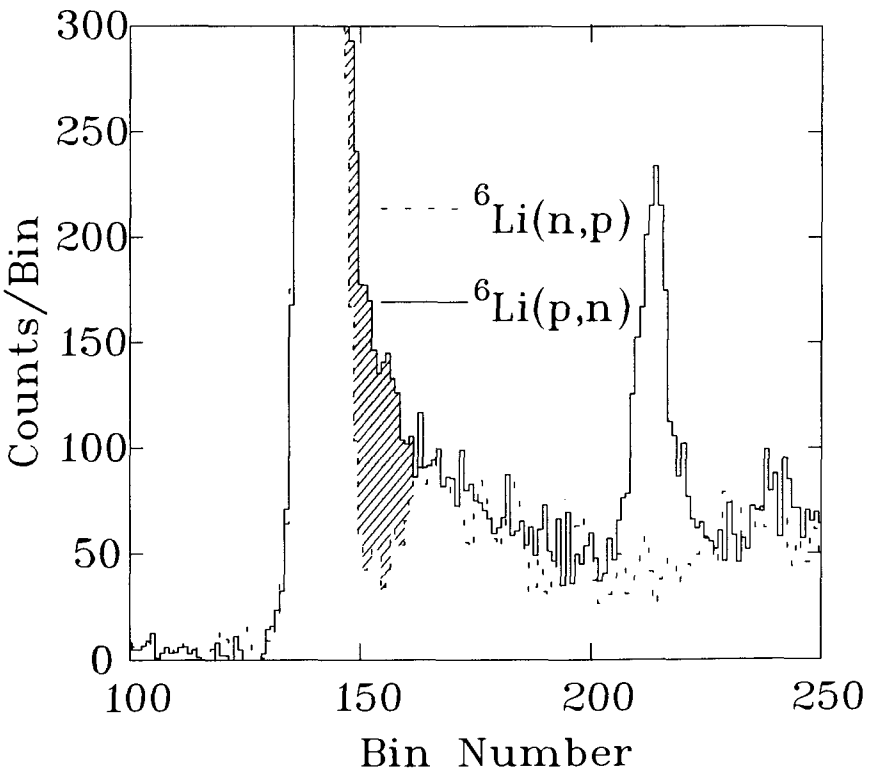

Figure 3.10: Spectra for ^{6}Li(n,p)^{6}He (dashed) and ^{6}Li(p,n)^{6}Be (solid). The (n,p) spectrum has been smoothed, shifted and scaled so the high-momentum side of the peak is normalized to the same region of the (p,n) peak, in order to obtain the contribution from the (p,n) "tail" (hatched area).

The technique for extracting the ^{6}Li(p,n)^{6}Be cross sections differs from the usual

method used in the analyses of (p,n) experiments, which is to compare (p,n) yields to that from the ^{7}Li(p,n)^{7}Be(g.s. + 429 keV first excited state) reaction. The 0° cross sections for this reaction have been obtained by Watson *et al* [28], who integrated the angular distribution at several energies between 198-400 MeV and normalized them to activation data by D'Auria *et al* [29]. Instead of comparing (p,n) yields with the ^{7}Li(p,n)^{7}Be reaction, we make use of a novel method of comparisons between ratios of yields from (n,p) and (p,n) reactions for ^{6}Li and ^{12}C. Denoting the yield per incident beam particle per target atom for primary target a and secondary target b by $Y(a,b)$:

$$R_1 = \frac{Y_{np}(^{7}\mathrm{Li},^{6}\mathrm{Li})}{Y_{np}(^{7}\mathrm{Li},^{12}\mathrm{C})} = \frac{\sigma_{np}^{^{6}Li}}{\sigma_{np}^{^{12}C}} \tag{3.26}$$

$$R_2 = \frac{Y_{pn}(^{6}\mathrm{Li},\mathrm{H})}{Y_{pn}(^{12}\mathrm{C},\mathrm{H})} = \frac{\sigma_{pn}^{^{6}Li}}{\sigma_{pn}^{^{12}C}} \tag{3.27}$$

Taking a ratio of these two quantities gives:

$$R = \frac{R_2}{R_1} = \frac{\sigma_{pn}^{^{6}Li}\sigma_{np}^{^{12}C}}{\sigma_{np}^{^{6}Li}\sigma_{pn}^{^{12}C}} \tag{3.28}$$

If we assume that the ratio $\sigma_{np}^{^{12}C}/\sigma_{pn}^{^{12}C}$ can be reliably predicted using DWIA calculations we can then obtain the ^{6}Li(p,n)^{6}Be cross section directly. The above procedure was adopted for both the 0° and 3° ^{12}C(n,p) points, and yielded ^{6}Li(p,n) cross sections consistent with each other to $< .7\%$. A test of this method is to compare our ^{12}C(p,n)^{12}N cross section with that of Watson *et al*, which is based on the ^{7}Li normalization. We find that our results are in good agreement, as can be seen in Fig. 3.11. Our normalization leads to consistency between the (p,n), (n,p) and (p,p′) cross sections, relative to the SP88 phase-shift solution.

Center of mass cross sections for (p,p′), (n,p) and (p,n) reactions on ^{12}C and ^{6}Li are given in Table 3.2 and Table 3.3, respectively.

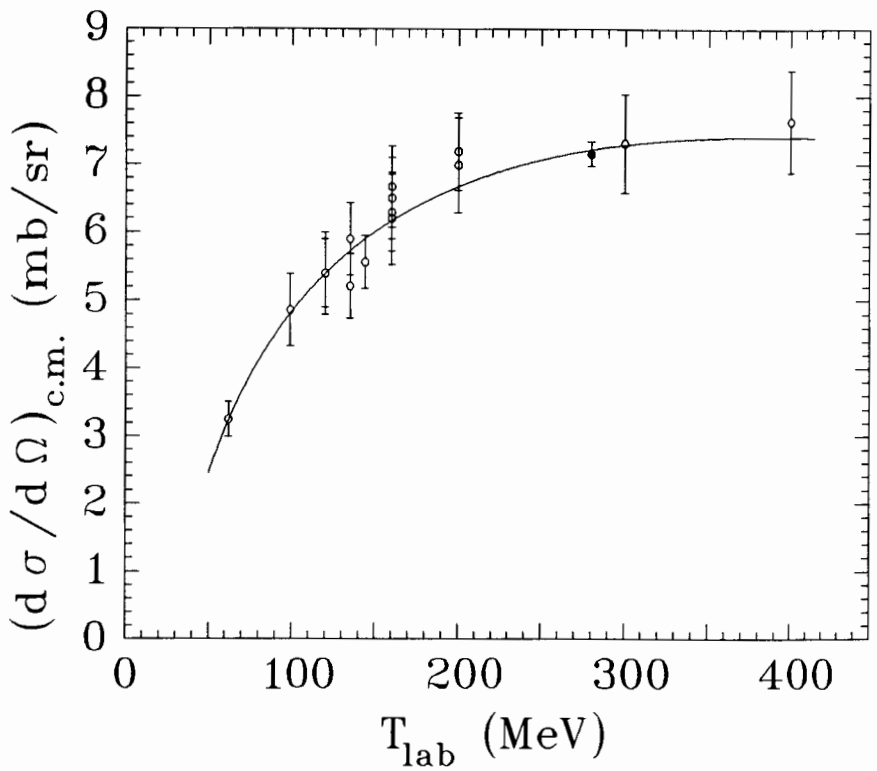

Figure 3.11: $^{12}C(p,n)^{12}N$ cross sections from Watson *et al*[28] as a function of incident proton energy. All points have been extrapolated to 0°. The curve is an empirical fit to Watson's and our data. The solid point is the result from this experiment; the error bar includes systematic uncertainties.

(p,p′)		(n,p)		(p,n)	
$\theta_{\text{c.m.}}$	$d\sigma/d\Omega_{\text{c.m.}}$	$\theta_{\text{c.m.}}$	$d\sigma/d\Omega_{\text{c.m.}}$	$\theta_{\text{c.m.}}$	$d\sigma/d\Omega_{\text{c.m.}}$
3.40	$2.903 \pm .071$	2.00	$7.43 \pm .08$	0.87	$7.08 \pm .09$
4.53	$2.311 \pm .060$	3.56	$5.89 \pm .08$		
5.40	$1.815 \pm .038$				
5.66	$1.780 \pm .049$				
6.52	$1.380 \pm .030$				
7.39	$1.105 \pm .035$				
7.65	$1.019 \pm .024$				
8.52	$0.802 \pm .030$				
9.41	$0.637 \pm .018$				
9.65	$0.641 \pm .027$				
10.54	$0.504 \pm .016$				
11.66	$0.356 \pm .017$				

Table 3.2: Center-of-mass cross sections for the reactions ^{12}C(p,p′)^{12}C, ^{12}C(n,p)^{12}B and ^{12}C(p,n)^{12}N at $T_{lab} = 280$ MeV. All cross sections are normalized to the SP88 phase shift solution. Angles are in degrees and cross sections in mb/sr (similarly for Table 3.3). Quoted errors are statistical only.

(p,p′)		(n,p)		(p,n)	
$\theta_{\text{c.m.}}$	$d\sigma/d\Omega_{\text{c.m.}}$	$\theta_{\text{c.m.}}$	$d\sigma/d\Omega_{\text{c.m.}}$	$\theta_{\text{c.m.}}$	$d\sigma/d\Omega_{\text{c.m.}}$
3.71	$5.373 \pm .085$	2.18	$13.20 \pm .14$	0.94	$14.67 \pm .33$
4.94	$4.134 \pm .067$	3.88	$10.76 \pm .15$		
5.89	$3.309 \pm .056$	7.30	$5.54 \pm .11$		
6.17	$3.134 \pm .053$	11.89	$1.69 \pm .06$		
7.12	$2.239 \pm .041$				
8.07	$1.746 \pm .043$				
8.35	$1.640 \pm .042$				
9.30	$1.145 \pm .032$				
10.27	$0.850 \pm .022$				
10.53	$0.772 \pm .030$				
11.49	$0.548 \pm .018$				
12.72	$0.353 \pm .016$				

Table 3.3: Center-of-mass cross sections for the reactions ^{6}Li(p,p′)^{6}Li, ^{6}Li(n,p)^{6}He and ^{6}Li(p,n)^{6}Be at $T_{lab} = 280$ MeV. All cross sections are normalized to the SP88 phase shift solution. Quoted errors are statistical only.

Chapter 4

Theoretical Calculations and Comparison with Experiment

The quantities required to fulfill the original aims of the experiment, the 0°, $q = 0$ $\vec{\sigma}\vec{\tau}$ matrix elements for the three different reactions, are strictly nuclear structure properties. The need to be able to theoretically model the reactions arises from the fact that the measured quantities (the reaction cross sections) are taken at finite values of q. In order to be able to extrapolate the cross section to 0° and $q = 0$ the q-dependence of the reactions must be understood over the experimentally accessible range. It should be emphasized that this experiment is not a 'test" of the nuclear structure model or the reaction model; rather, the theory calculations are required to be able to make meaningful comparisons between cross sections measured at different values of q as well as providing an extrapolation to non-physical values of q.

As stated in Chapter 1, the DWIA calculations require as input the nuclear structure parameters, the dynamics and q-dependence of the nuclear interaction and optical potentials which describe the macroscopic scattering properties of the nucleus. This chapter will describe in more detail how the various parts of the DWIA model are obtained, the specific details of the parameters used for modeling

the A=12 and A=6 systems, and then compare the experimental results with the theoretical calculations. Following this will be a discussion of some of the aspects of the measurements and theoretical calculations which affect the reliability of the results.

4.1 Shell Model Calculations

In the absence of many-body forces the nuclear Hamiltonian may be written as:

$$H = \sum_i T(\vec{r}_i) + \sum_i \sum_{j>i} V(\vec{r}_i, \vec{r}_j) \tag{4.1}$$

where $\vec{r}_i$ is the radius vector of the i^{th} nucleon from the nuclear center, $T(\vec{r}_i)$ is the single particle kinetic energy operator, and $V(\vec{r}_i, \vec{r}_j)$ is the two-body NN potential. We can rewrite the second term as

$$\sum_i \sum_{j>i} V(\vec{r}_i, \vec{r}_j) = \sum_i V_0(\vec{r}_i) + \left[\sum_i \sum_{j>i} V(\vec{r}_i, \vec{r}_j) - \sum_i V_0(\vec{r}_i) \right] \tag{4.2}$$

The term in square brackets is assumed to be small enough to be treated by perturbation theory. The Hamiltonian is now

$$H = H_0 + H_{res} \tag{4.3}$$

where

$$H_0 = \sum_i T(\vec{r}_i) + \sum_i V_0(\vec{r}_i) \tag{4.4}$$

is the single particle Hamiltonian and

$$H_{res} = \left[\sum_i \sum_{j>i} V(\vec{r}_i, \vec{r}_j) - \sum_i V_0(\vec{r}_i) \right] \tag{4.5}$$

In general, shell model calculations work with the energy relative to a closed shell rather than the total energy of the system. By considering ground state binding energies relative to the closed shell (assumed to be inert) and energy levels of states

with well-determined angular momentum (J) and isospin (T) quantum numbers, a fit can be done to determine the two-body residual matrix elements between states in the valence shell. Nuclear wave functions can then be determined from these matrix elements, usually under the assumption that there are no admixtures of states from outside the valence shell. Cohen and Kurath [31] followed this procedure to obtain the two-body matrix elements for the 1p shell.

The wave functions for the calculations to be described below are calculated from two sets of 1p two-body matrix elements, derived under slightly different assumptions. The A=12 calculations use the 8-16 POT matrix elements. As the name suggests, these use input data from nuclei in the range A=8–16, and are calculated in the LS coupling representation. The A=6 calculations use the 6-16 2BME set, calculated in the jj coupling representation. The main difference, apart from the input data used, is that the 8-16 POT fit assumes that the radial wave functions are the same for $1p_{3/2}$ and $1p_{1/2}$ orbitals, whereas the 6-16 2BME fit does not. To test the validity of the derived matrix elements the energy levels and other nuclear properties (e.g. the magnetic dipole moment) can be calculated for the various nuclei and compared with the experimentally determined values. In each case the set used was the one that gave a better fit of the energy levels of the given nucleus.

The computer code OXBASH [39] was used to calculate the nuclear wave functions and the one-body transition densities between the states. In the "second quantization" formalism the Hamiltonian operator H between the many-particle basis wave functions can be written as

$$H = H_{\text{core}} + \sum_i \epsilon_i a_i^+ a_i + \sum_j \sum_{i>j} \sum_l \sum_{k>l} v_{ijkl} a_i^+ a_j^+ a_l a_k \qquad (4.6)$$

where ϵ_i is the energy of a single-particle state, a_i^+ (a_i) is the creation (annihilation)

operator for single-particle state with the set of quantum numbers labeled by i, and

$$v_{ijkl} = \langle ij|V|kl\rangle \tag{4.7}$$

The two-particle states $|ij\rangle$ have been antisymmetrized and are obtained from

$$\begin{aligned}
\langle 12|V|34\rangle &\equiv \langle j_1\ m_1\ t_{z1}\ j_2\ m_2\ t_{z2}|V|j_3\ m_3\ t_{z3}\ j_4\ m_4\ t_{z4}\rangle \\
&= \frac{1}{[(1+\delta_{12})(1+\delta_{34})]^{1/2}} \sum_{J,T} \langle j_1\ j_2|V|j_3\ j_4\rangle^{JT} \\
&\quad \times \langle j_1\ m_1\ j_2\ m_2|J\ m1+m2\rangle \langle j_3\ m_3\ j_4\ m_4|J\ m3+m4\rangle \\
&\quad \times \langle 1/2\ t_{z1}\ 1/2\ t_{z2}|T\ t_{z1}+t_{z2}\rangle \langle 1/2\ t_{z3}\ 1/2\ t_{z4}|T\ t_{z3}+t_{z4}\rangle
\end{aligned} \tag{4.8}$$

Here, the matrix elements $\langle j_1\ j_2|V|j_3\ j_4\rangle^{JT}$ are those determined by Cohen and Kurath.

The initial and final nuclear states are specified by the number of valence particles and the angular momentum and isospin quantum numbers, J and T. States with good J and T are projected from a basis set constructed using an m-scheme Slater determinant. The Hamiltonian matrix is then constructed from the allowed states and diagonalized, which gives the eigenvalues (the single particle energies) and eigenfunctions (the nuclear wave functions).

What is actually required from the shell model calculations as input for the DWIA calculation are the one-body transition densities (OBTD's). Although in general the calculations are done for many particle states, the main steps can be explained in a straightforward manner by considering only two particles. Starting with the antisymmetrized m-scheme wave functions (considering the angular momentum only)

$$|j_m j'_{m'}\rangle = a^+_{j'm'} a^+_{jm} |\rangle \tag{4.9}$$

where $|\rangle$ is the vacuum state. For two particles coupled to J the antisymmetrized

wave function (normalized to unity) is

$$\begin{aligned} |jj'JM\rangle &= \frac{1}{(1+\delta_{j,j'})^{1/2}} \sum_m \sum_{m'} \langle jmj'm'|JM\rangle a^+_{j'm'} a^+_{jm} |\rangle \\ &= -\frac{1}{(1+\delta_{j,j'})^{1/2}} [a^+_j \otimes a^+_{j'}]^{JM} |\rangle \end{aligned} \tag{4.10}$$

We make use of the Wigner-Eckart theorem which states that

$$\langle JM|T^{(k)}_q|J'M'\rangle = \frac{\langle J'M'kq|JM\rangle \langle J||T^{(k)}||J'\rangle}{(2J+1)^{1/2}} \tag{4.11}$$

where $T^{(k)}_q$ is a spherical tensor operator of rank k and $\langle J||T^{(k)}||J'\rangle$ is the reduced matrix element, which is independent of M and M'. Now, labelling the single-particle state quantum numbers by ρ and denoting the many-particle state with angular momentum J and isospin T by $|\Gamma\rangle$ we can define the OBTD for two states coupled to spin and isospin λ as

$$\mathrm{OBTD}(\rho, \rho'; \lambda) = \frac{1}{(2\lambda+1)^{1/2}} \langle \Gamma ||| [a^+_\rho \otimes \tilde{a}_{\rho'}]^\lambda ||| \Gamma' \rangle \tag{4.12}$$

where $\tilde{a}_\rho$ is a tensor operator which creates the "hole" state $|\rho^{-1}\rangle$; it is related to the standard particle annihilation operator by

$$\tilde{a}_{j,m} = -(1)^{j+m} a_{j,-m} \tag{4.13}$$

The three bars denote a "doubly reduced" matrix element, i.e. one that has been reduced in both spin and isospin. The input to DW81 actually requires that the OBTD's be modified by a factor of

$$Z_{\mathrm{DW81}} = \mathrm{OBTD}_{\mathrm{OXBASH}} \times \langle T_i \; T_{i3} \; T \; T_3 | T_f \; T_{f3} \rangle \frac{\hat{T}}{\hat{J}_i \hat{T}_f} \tag{4.14}$$

where T_i (T_f) is the isospin quantum number of the initial (final) state; T is the change of isospin, and $\hat{T} \equiv \sqrt{2T+1}$ (similarly for J).

The number of transition densities required depends on the number of particles in the valence shell and the type of transition. A particularly simple case is ^{6}Li,

which has just two valence particles (1 proton and 1 neutron). The proton (or neutron) is either in a $p_{3/2}$ or a $p_{1/2}$ orbital. Because there are no filled sub-shells there are no restrictions on the transitions; and because there are only two valence particles there is only one possible particle-hole coupling for a particular single-particle transition. So we are left with only four transition densities corresponding to the transitions $p_{1/2} \rightarrow p_{1/2}$, $p_{1/2} \rightarrow p_{3/2}$, $p_{3/2} \rightarrow p_{1/2}$ and $p_{3/2} \rightarrow p_{3/2}$. Binding energy differences will in principle make the transition densities differ depending on whether the reaction is (p,p'), (n,p) or (p,n), and (for (p,p') reactions) whether the nucleon participating in the reaction is a proton or a neutron. The nuclear structures of ^{6}He and ^{6}Be are not very well known. Consequently, the transition densities used are the same for all three reactions, that is, they assume that isospin symmetry is conserved.

The situation for ^{12}C is more complicated. There are eight valence particles (four protons and four neutrons) so the number of ways the single-particle states can couple to form the many-particle states is increased. There are also restrictions on some of the single-particle transitions because of filled sub-shells. Six transitions are allowed amongst nine single-particle states for both the protons and the neutrons. In addition the (p,p') transition densities have been modified to include the (small) effects of isospin mixing between the 15.11 MeV $J^\pi=1^+;T=1$ and the 12.71 MeV $J^\pi=1^+;T=0$ states in ^{12}C [40]. This mixing was determined from (e,e') scattering data and is expressed as

$$|15.11 \text{ MeV}\rangle = \sqrt{1-\beta^2}|T=1\rangle + \beta|T=0\rangle \tag{4.15}$$

where

$$\beta = \frac{\langle T=1|H_{CD}|T=0\rangle}{\Delta E} = \frac{.140 \pm .035 \text{ MeV}}{2.4 \text{ MeV}} = .0583 \pm .015 \tag{4.16}$$

The $T = 1$ transition densities are modified by

$$\mathrm{OBTD}_{15.11\ \mathrm{MeV}} = \mathrm{OBTD}_{T=1} - \beta \times \mathrm{OBTD}_{T=0} \tag{4.17}$$

In practice the difference in calculated cross sections is negligible using corrected and uncorrected transition densities. The numerical values of these coefficients for A=6 and A=12 are given in Table 4.1. There are two transition densities for each of the $j_i = 3/2$ initial states in A=12 due to coupling to different A=11 parent states.

		Z_{DW81}			
		$A = 6$	$A = 12$		
			(n,p);(p,n)	(p,p′)	
$2j_f$	$2j_i$			pp^{-1}	nn^{-1}
1	1	.029	.0581	.0605	-.0554
1	3	.187	.7098	.6654	-.7517
			-.0195	-.0183	.0207
3	1	-.197	.3394	.3182	-.3595
3	3	.191	.2895	.2857	-.2922
			-.2131	-.2103	.2151

Table 4.1: Transition densities used in the DWIA calculations. The notation pp^{-1} (nn^{-1}) specifies proton (neutron) transitions.

4.2 The Love-Franey Effective Interaction

Any possible formulation of the NN interaction must be some combination of Lorentz scalar quantities that are all invariant under parity, time reversal and coordinate rotation transformations. Of the 18 such quantities that can be formed from various combinations of the spin (σ) angular momentum ($\mathbf{L}$) and isospin (τ) vectors only 5 are linearly independent; each of these can have isoscalar and isovector components for a total of 10 terms. In most treatments two of these terms, the

quadratic spin-orbit terms (isoscalar and isovector) are neglected, leaving:

$$V_{12} = V_0^C(\mathbf{r}) + V_\sigma^C(\mathbf{r})\boldsymbol{\sigma}_1 \cdot \boldsymbol{\sigma}_2 + V_\tau^C(\mathbf{r})\boldsymbol{\tau}_1 \cdot \boldsymbol{\tau}_2 + V_{\sigma\tau}^C(\mathbf{r})\boldsymbol{\sigma}_1 \cdot \boldsymbol{\sigma}_2\boldsymbol{\tau}_1 \cdot \boldsymbol{\tau}_2$$

$$+V^{LS}(\mathbf{r})\mathbf{L} \cdot \mathbf{S} + V_\tau^{LS}(\mathbf{r})\mathbf{L} \cdot \mathbf{S}\boldsymbol{\tau}_1 \cdot \boldsymbol{\tau}_2$$

$$+ V^T(\mathbf{r})S_{12} + V_\tau^T(\mathbf{r})S_{12}\boldsymbol{\tau}_1 \cdot \boldsymbol{\tau}_1 \tag{4.18}$$

where $\mathbf{r} = \mathbf{r}_{12}$ is the radius vector joining the two nucleons, $\mathbf{L} \cdot \mathbf{S}$ is the spin-orbit operator for relative angular momentum $\mathbf{L}$ and

$$\mathbf{S} = \frac{1}{2}(\boldsymbol{\sigma}_1 + \boldsymbol{\sigma}_2) \tag{4.19}$$

The tensor operator S_{12} is defined as

$$S_{12} = 3(\boldsymbol{\sigma}_1 \cdot \hat{r})(\boldsymbol{\sigma}_2 \cdot \hat{r}) - \boldsymbol{\sigma}_1 \cdot \boldsymbol{\sigma}_2 \tag{4.20}$$

The starting point for building up the effective interaction is to determine the phase shifts and scattering amplitudes ($f(E_{c.m.}, \theta)$) from a partial wave analysis of NN scattering data over a wide range of energies [41]. This analysis expresses the measured NN cross sections as a sum of terms for different angular momentum channels (e.g. triplet-odd, triplet even etc.) and determines the phase shift δ and scattering amplitude for each term[1]. The free ("on-shell") NN t-matrix is constructed from the extracted scattering amplitudes [37]:

$$t_{NN}(E_{c.m.}, \theta) = \eta f(E_{c.m.}, \theta) \tag{4.21}$$

where

$$\eta = \frac{-4\pi(\hbar c)^2}{E_{c.m.}}, \qquad E_{c.m.}^2 = m^2c^4 + (\hbar ck)^2 \ , \tag{4.22}$$

m is the nucleon mass and $\hbar k$ is the momentum of either nucleon in the center of momentum frame.

[1]This is essentially the same data set used to determine the H(p,p) and H(n,p) cross sections to which the data from this experiment are normalized.

Except for the tensor pieces, all terms of the potential are assumed to have a radial dependence given by Yukawa functions, e.g.

$$V^C(r) = \sum_{i=1}^{N} V_i^C \frac{e^{-\mu_i r}}{\mu_i r} \tag{4.23}$$

where the μ_i are range parameters and the sum extends to a maximum of 4. The tensor pieces are described by $r^2 \times$Yukawa terms. The ranges and amplitudes for each NN angular momentum channel are fit to the experimentally derived NN t-matrix according to

$$t_{NN}(E,q) = \int d^3r e^{-i\vec{k}\cdot\vec{r}} V_{12}[1 + (-)^l P_x] e^{i\vec{k}\cdot\vec{r}} \tag{4.24}$$

where P_x is the space-inversion (parity) operator; the term $(-)^l P_x$, where l is the relative angular momentum in the NN system, ensures antisymmetrization. To use the derived effective interaction in the N-nucleus (NA) system it is necessary to rescale t_{NN} kinematically by an amount

$$t_{NA} = \frac{\epsilon_0^2}{\epsilon_p \epsilon_t} t_{NN} \tag{4.25}$$

where ϵ_0 is the total energy of the incident nucleon in the NN center of momentum system and ϵ_p (ϵ_t) is the total energy of the incident (target) nucleon in the NA center of momentum frame.

4.3 Optical Potentials

The inelastic part of the N-nucleus interaction at small angles is almost always small enough to be treated as a perturbation to the dominant process of elastic scattering. In the DWIA model the gross features of the nucleus encountered by the incoming nucleon are in the form of an optical potential which has terms that reflect the total elastic and inelastic scattering amplitudes:

$$V_{opt} = U(r) + iW(r) = U_O f_R(r) + iW_O f_I(r) \tag{4.26}$$

where the potential contains both central and spin-orbit terms. It is assumed that the features of the nuclear force are essentially the same in the nucleus as they are for free nucleons, with the radial strength of the interaction proportional to the local nuclear density. Thus, the optical potentials are generated by folding the effective NN interaction with the nuclear density distributions.

Charge distributions for nuclei can be found from measuring the electromagnetic form factors determined from (e,e) scattering: the charge distribution is simply the Fourier transform of $F(q^2)$. Many nuclear charge distributions can be fit vary well to a "3-parameter Fermi" (3pF) distribution of the form

$$\rho(r) = \rho_0 \frac{1 + wr^2/c^2}{1 + e^{(r-c)/z}} \tag{4.27}$$

What is required for obtaining the optical potential is not the charge distribution but the matter distribution. Since the proton itself is not a point particle but actually an extended charge source it is necessary to "unfold" the finite charge distribution of the protons from the measured charge distribution. The matter distribution of neutrons was assumed to be the same as that for protons for both ^{6}Li and ^{12}C.

In general the optical potentials for the entrance channel for a reaction differ from those of the exit channel because the nuclear structures are different. The relative importance of this difference decreases with larger-A nuclei; thus we would expect that the difference in the entrance and exit channel optical potentials to be more important for reactions on ^{6}Li than for ^{12}C. For this reason the matter distributions used for both entrance and exit channel optical potentials were the same for the $A = 12$ reactions. That is, the shapes of the charge distributions for ^{12}N and ^{12}B were assumed to be the same as for ^{12}C, with the total charge normalized to $7e$ and $5e$, respectively. For the $A = 6$ reactions an attempt was made to include the differences in the matter distributions. The problem with this

is that empirical charge distributions are not available for unstable nuclei such as ^{6}Be and ^{6}He. Instead it was assumed that ^{6}Be had the same proton distribution as Be^9 and the same neutron distribution (assumed to be the same as the proton distribution) as ^{4}He; and that ^{6}He had proton distribution of ^{4}He, with the neutron distribution taken to be the same as the protons of ^{9}Be.

The ^{12}C charge distribution [42] was obtained from (e,e) data over a range of $q = .25$–2.3 fm^{-1} fit directly to a 3pF distribution. The charge distribution for ^{6}Li [43], from a range of $q = .56$–3.66 fm^{-1}, was originally fit to a phenomenological function

$$\rho(r) = \frac{Z}{8\pi^{3/2}}\left[\frac{1}{a^3}e^{-r^2/4a^2} - \frac{c^2(6b^2 - r^2)}{4b^7}e^{-r^2/4b^2}\right] \tag{4.28}$$

from which a 3pF function was then fit. The He^4 charge distribution [44] was from a direct 3pF fit to data over the range $q = .59$–2.5 fm, while the Be^9 distribution was obtained from a 3pF fit to a harmonic oscillator parameterization of data covering a range of $q = .26$–$.7$ fm [45].

The matter distributions unfolded from the charge distributions were also parameterized as 3pF distributions. Values of the parameters for both the charge and matter distributions used for the $A = 6$ entrance channel and $A = 12$ (entrance and exit channel) optical potentials are listed in Table 4.2 Exit channel parameters for the $A = 6$ charge exchange reactions are listed in Table 4.3.

The optical potentials are generated by the program MAINX8 [46] which also includes Coulomb effects to take into account whether the incident and scattered particle are protons or neutrons. The (p,p′) reaction cross section for ^{6}Lifrom the derived optical potential (138 mb) is in reasonable agreement with the experimental value (149 ± 3 mb) [47] measured at 180 MeV, while the calculated (p,p′) reaction cross section for ^{12}C (226 mb) also agrees well with the experimental value (199 ± 20

	$A = 6$		$A = 12$	
	Charge	**Matter**	**Charge**	**Matter**
c (fm)	1.3439	1.1047	2.3550	2.1883
z (fm)	0.5557	0.5856	0.5224	0.5126
w	0.0996	0.0242	-0.1490	-0.1448
$\langle r^2 \rangle^{1/2}$ (fm)	2.553	2.448	2.455	2.324

Table 4.2: Experimental charge and matter distributions used to obtain the entrance (entrance and exit) channel optical potentials for $A = 6$ ($A = 12$) DWIA calculations. The parameters are from 3pF fits to the charge distributions. See text for further details.

	^{9}Be (protons in ^{6}Be, neutrons in ^{6}He)		**^{4}He** (protons in ^{6}He, (neutrons in ^{6}Be)	
	Charge	**Matter**	**Charge**	**Matter**
c (fm)	2.1464	1.927	0.964	1.0391
z (fm)	0.6547	0.6446	0.322	0.3268
w	-0.1445	-0.1275	0.517	0.0985
$\langle r^2 \rangle^{1/2}$ (fm)	2.523	2.464	1.747	1.554

Table 4.3: Experimental charge and matter distributions used to obtain the exit channel optical potentials for $A = 6$ DWIA calculations. See text for further details.

mb) [48] measured at 290 MeV.

4.4 DWIA Calculations

The reaction cross section calculated in the DWIA model is

$$\frac{d\sigma}{d\Omega} = (\frac{\mu}{\pi\hbar^2})^2 \frac{k_i}{k_f} \frac{1}{2} \frac{|T^{DW}|^2}{2J+1} \tag{4.29}$$

where μ is the relativistically-reduced energy, J is the final-state angular momentum and k_i (k_f) is the wavenumber of the incident (scattered) particle. The reaction transition matrix T^{DW} is expressed as a sum of terms corresponding to the different pieces of the nuclear force, e.g. scalar, τ, $\vec{\sigma}\vec{\tau}$, etc.:

$$T^{DW} = \sum_{\alpha} \int d^3q D_\alpha(\mathbf{k}, \mathbf{k}'; \mathbf{q}) V_\alpha(\mathbf{q}) \rho^\alpha_{fi}(\mathbf{q}) \tag{4.30}$$

The potential $V_\alpha(\mathbf{q})$ is the momentum space representation of the effective interaction described above, obtained by a Fourier transform. The distortion factor $D_\alpha(\mathbf{k}, \mathbf{k}'; \mathbf{q})$ gives the overlap of the incoming ($\chi^{(+)}_{i,\mathbf{k}}$) and outgoing ($\chi^{(-)}_{f,\mathbf{k}'}$) distorted waves for component α of the N-nucleus interaction

$$D_\alpha(\mathbf{k}, \mathbf{k}'; \mathbf{q}) = \frac{1}{(2\pi)^3} \langle \chi^{(-)}_{f,\mathbf{k}'} | e^{-i\mathbf{q}\cdot\mathbf{r}_p} \mathrm{Op}^\alpha(\mathbf{q}) | \chi^{(-)}_{f,\mathbf{k}'} \rangle \tag{4.31}$$

where $\mathbf{r}_p$ is the radius vector for the target nucleon and $\mathrm{Op}^\alpha(\mathbf{q})$ is the operator for component α of the interaction. The distorted waves are calculated by solving the Schrödinger equation with the Coulomb-modified optical potentials described above

$$\left\{ \nabla^2 + k^2 - (2\mu\hbar^2) \left[V_{opt}(\mathbf{r}) + V_{coul}(\mathbf{r}) \right] \right\} \chi_{\mathbf{k}}(\mathbf{r}) = 0 \tag{4.32}$$

The final factor is the nuclear transition density

$$\rho^\alpha_{fi}(\mathbf{q}) = \langle \Psi_f | \sum_i e^{-i\mathbf{q}\cdot\mathbf{r}_p} \mathrm{Op}^\alpha(\mathbf{q}) | \Psi_i \rangle \langle N_i | \mathrm{Op}^\alpha(\mathbf{q}) | N_f \rangle \tag{4.33}$$

where the first matrix element is the product of the shell model transition density and the overlap of the initial and final radial wave functions and the second is the volume integral of the NN effective interaction.

The only parts of the DWIA calculations which have not yet been specified are the single-particle radial wave functions. The two most commonly used forms for the radial dependence of the potential are the Woods-Saxon form

$$V^{W.S.}(r) = -\frac{V_0}{1 + e^{(r-R_0)/a}} \tag{4.34}$$

and the Harmonic Oscillator form

$$V^{H.O.} = -V_0 \left[1 - \left(\frac{r}{R_0}\right)^2\right] = \frac{m}{2}\omega_0^2(r^2 - R_0^2) \tag{4.35}$$

where $R_0 = r_0 A^{1/3}$ and $r_0 \simeq 1.2$ fm. While the Woods-Saxon potential is generally believed to be a more realistic shape than the Harmonic Oscillator potential, its eigenfunctions cannot be expressed in a closed form. The H.O. potential has analytic solutions for the eigenfunctions and the radial overlap integral. For many applications the H.O. and W.S. potentials give very similar results.

The H.O. potential is specified in terms of a single parameter

$$b = \sqrt{\frac{\hbar}{m\omega_0}} \tag{4.36}$$

which can be adjusted to fit the shape of the angular distribution. The use of a single parameter for all three types of reaction will cause the radial overlap integral to be identical (unity) in all three cases. This is equivalent to assuming that the single-particle binding energies are the same in all three members of the final state multiplet.

The W.S. well depth is determined empirically by a fit to the binding energies of the single-particle states, with the other parameters for the W.S. potential obtained

from fits to electron scattering data [49]. Thus if the single-particle binding energies can be reliably specified for all three members of the final state multiplet, there can be differences in the radial overlap integral which will be reflected in the reaction cross sections.

4.5 Comparison of Data with Calculations

In Fig. 4.3 the cross sections for the A=12 system are compared with calculations which include the effects of isospin breaking explicitly in the form of binding energy differences between members of the final state multiplet. The calculations reproduce exactly the observed ft asymmetry but require a normalization factor of 1.2 to obtain agreement with the absolute B(GT) values. An overall normalization factor of 1.3 was applied to the reaction calculations to force agreement with the low-q (p,p′) data.

The large range of scattering angles for the (n,p) reactions made it necessary to fold the theoretical (n,p) angular distribution with the experimental MRS angular acceptance. For each MRS angle setting the angular acceptance was approximated by a Gaussian function whose width varied linearly between angles to reflect the changing shape of the acceptance curve. The theoretical distribution was convoluted at each angle with a Gaussian of the appropriate width. The effect of this procedure is greatest where there is the most slope; the theoretical distribution tends to flatten out as a result. The (n,p) scattering angle distributions for MRS angles 0°, 3°, 6° and 10° are shown in Fig. 4.1. The effects of the convolution on the theoretical (n,p) curves are shown in Fig. 4.2.

The (p,n) datum was taken, according to the procedure outlined in Chapter 3, to be the average of the values calculated with the two 280 MeV (n,p) data points,

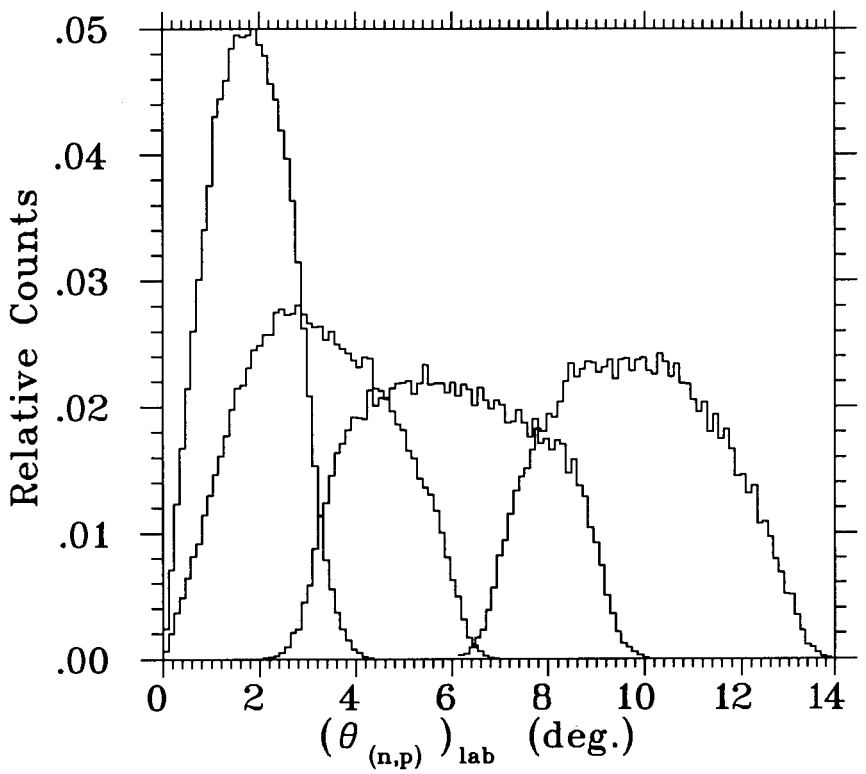

Figure 4.1: (n,p) scattering angle distributions for MRS settings of 0°, 3°, 6° and 10°. The distributions were approximated by Gaussians and folded with the theoretical (n,p) curves.

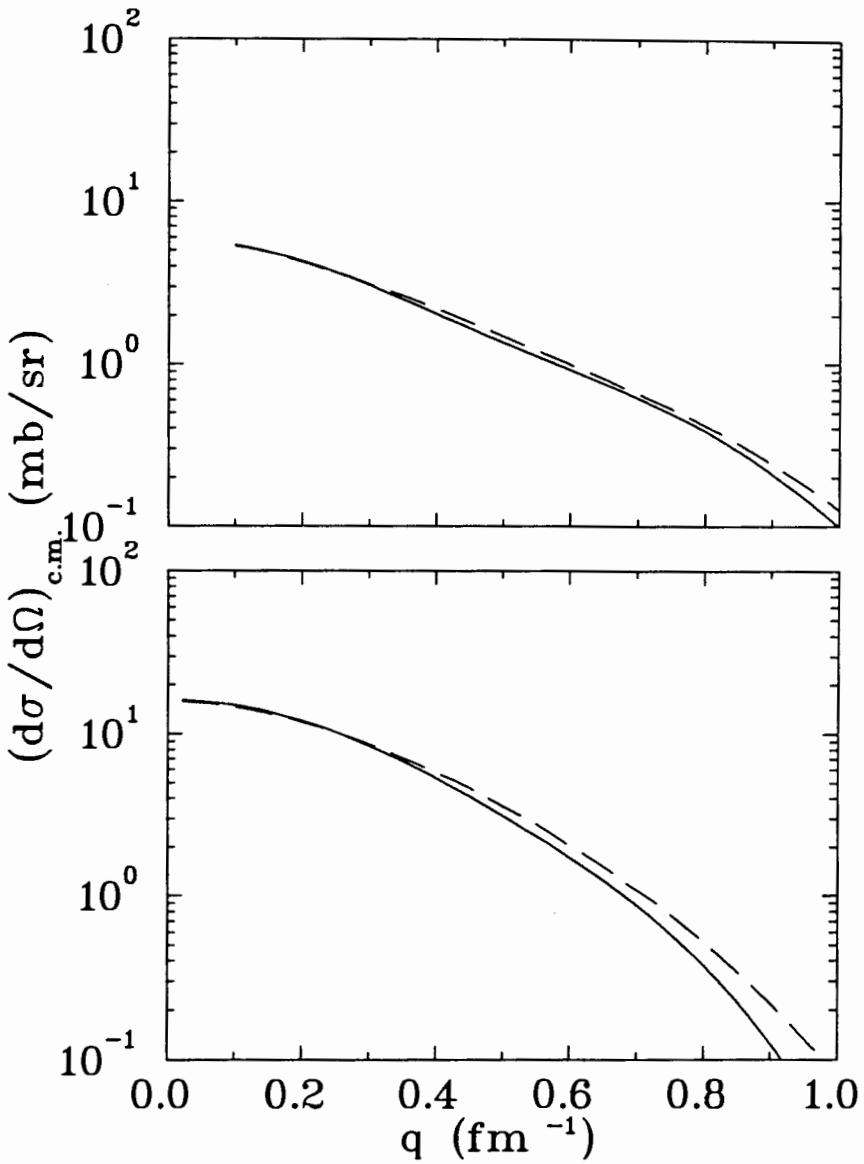

Figure 4.2: Theoretical (n,p) curves convoluted with experimental scattering angle distributions for ^{12}C(n,p) (top) and ^{6}Li(n,p) calculations. The solid lines are the original calculations; the dashed lines are after convolution.

assuming that the reaction preserves the isospin asymmetry observed in the B(GT) values. Because of the scarcity of (n,p) and (p,n) data at 280 MeV we also show an angular distribution (theory dashed) previously measured at 200 MeV [50]. The ratio of $\sigma_{exp}/\sigma_{theo}$ is shown at the bottom of Fig 4.3. The SP88 normalization implies that the (n,p) data are compatible with the (p,p′) data to an accuracy of about ±3%. The (p,p′) angular distribution falls off more rapidly with momentum transfer than the calculation; since realistic radial form factors were used this could be attributed to the effective interaction, although the origin may also lie in the Cohen and Kurath transition densities. Experimental cross sections for the 280 MeV data of Fig. 4.3 are given in Table 3.2.

The calculations for $A = 6$ differed somewhat from those for $A = 12$. Since the ^{6}Be ground state is unbound to particle emission B(GT$^+$) is not available and therefore isospin symmetry was assumed in the theoretical calculations. An attempt was made to model the A=6 reactions with Woods-Saxon radial form factors (with no adjustable parameters) as was done for A=12. This procedure yielded angular distributions that agreed very poorly with the data for both (n,p) and (p,p′) reactions. This technique may not be suitable for A=6 nuclei because the A=5 parent states relative to which the binding energies are determined are themselves unbound. Instead, the radial form factors were obtained with a harmonic oscillator potential whose size parameter was adjusted to a large value (b = 2.15 fm) to force agreement with the (p,p′) angular distribution; for the (n,p) and (p,n) calculations the same oscillator parameter was adopted. It should be emphasized that, unlike the calculations for A=12, this procedure did not include any known isospin symmetry-breaking effects (i.e. binding energy differences) *a priori*: rather, any such effects would be revealed as discrepancies between theory and data.

The data for the three reactions, which have been normalized in the same way

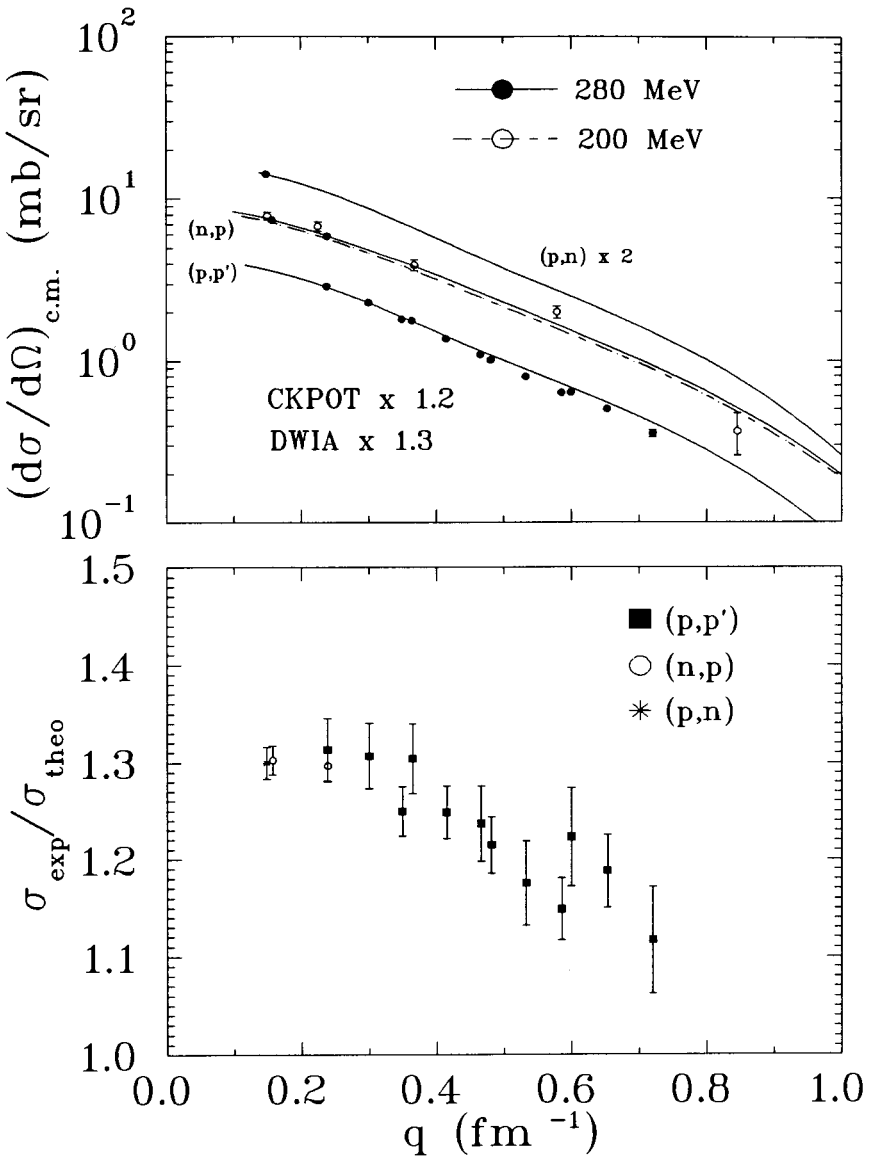

Figure 4.3: Angular distributions for the ^{12}C(p,n) and (p,p') reactions at 280 MeV and the (n,p) reaction at 200 [50] and 280 MeV populating the A=12, 1^+ isospin triad (top). The theoretical curves are DWIA calculations which incorporate known isospin breaking effects (see text). The curves include the effects of finite angular acceptance which differ markedly for the three reactions. Also shown (bottom) are the ratios of experimental to theoretical cross sections for all three reactions.

as those for the A=12 system, and theoretical calculations are shown in Fig. 4.4. The calculations have to be multiplied by a factor of 0.88 to reproduce B(GT$^-$), and with this are in very good agreement with the (p,p′) data. The (p,p′) data fall below the (n,p) and (p,n) data by several per cent at finite values of q. In order to get a quantitative measure of this apparent asymmetry, the mean value of the ratio of experimental to theoretical cross sections ($\bar{r}$) for the four most forward angle (p,p′) points can be compared to a "CHARGEX" average consisting of the mean value of the same ratio for the (p,n) datum and the two most forward angle (n,p) data, with the result that the CHARGEX ratios exceed the (p,p′) ratios by

$$\delta_{A=6} = \bar{r}_{CHARGEX}/\bar{r}_{(\mathrm{p,p'})} - 1 = .051 \pm .024 \tag{4.37}$$

However, we note that upon extrapolation to $q = 0$ the asymmetry may become negligible. The corresponding ratio for the A=12 system (which does not include the (p,n) datum) is

$$\delta_{A=12} = .005 \pm .028 \tag{4.38}$$

Theoretical estimates of isospin breaking in the A=6 system are, however, difficult because of the low two-particle emission thresholds (see Fig. 1.2), the particle instability of ^{6}Be, and the cluster-like structure of the ^{4}He+2N system. Experimental cross sections for the 280 MeV data of Fig. 4.4 are given in Table 3.3. The discrepancy of the ^{6}Li(n,p) points with the theoretical curve, which increases with q, is in part attributable to the (partially) unresolved, J$^\pi$=2$^+$;T = 1 ^{6}He state at 1.8 MeV, but estimates based on an anlaysis of ^{6}Li(n,p) data taken at 200 MeV [51] suggest that this contribution is $\leq$ 0.5% at $\theta_{MRS} = 0°$, and no more than 1% at $\theta_{MRS} = 6°$.

The obvious question to ask is whether the effect observed in the A = 6 triad is a real indication of isospin symmetry breaking, the result of some systematic or

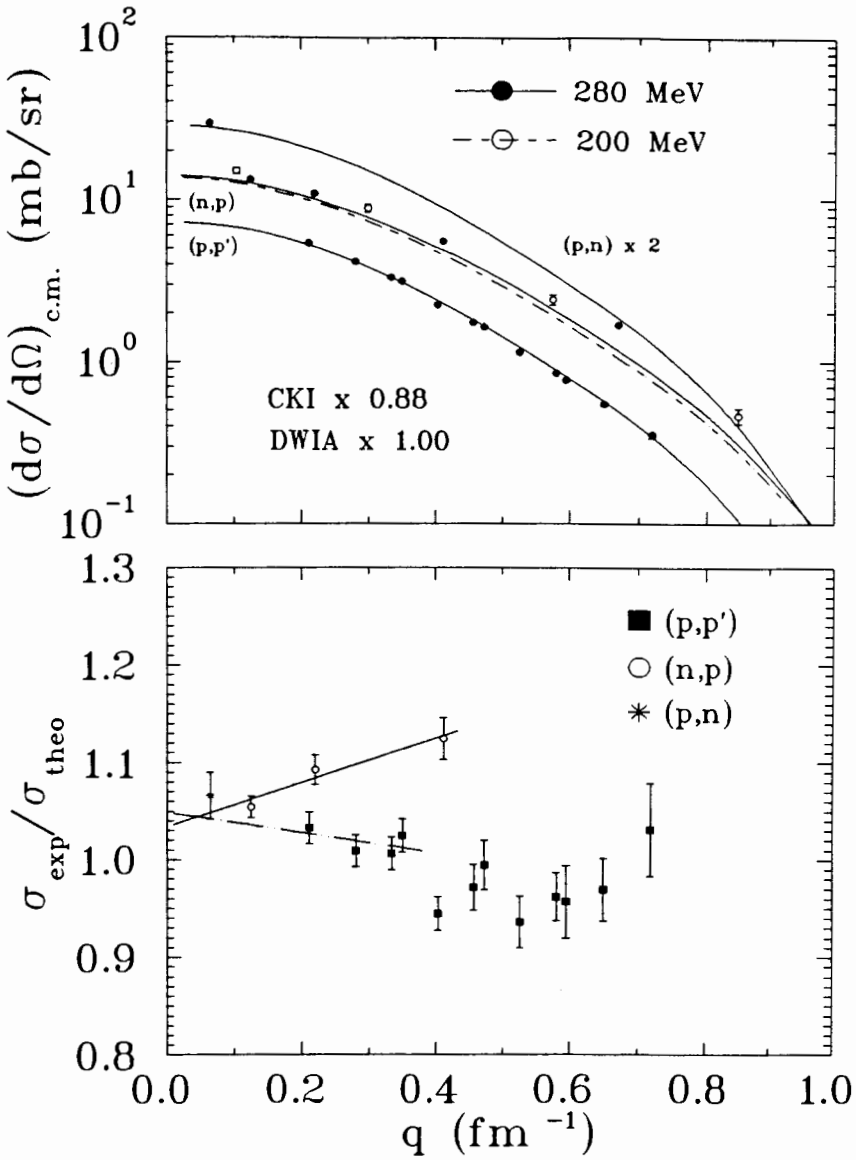

Figure 4.4: Angular distributions for the ^{6}Li(p,n) and (p,p') reactions at 280 MeV and the (n,p) reaction at 200 [50] and 280 MeV populating the A=6, 0^+ isospin triad. The theoretical DWIA curves assume good isospin in the three reactions and include the effects of finite angular acceptance in the experiments. Also shown (bottom) are the ratios of experimental to theoretical cross sections for all three reactions. The dashed line is a linear extrapolation from the forward angle (p,p') data; the solid line is an extrapolation from the CHARGEX data.

measurement uncertainty in the data, or a wrong or imprecise assumption in the theoretical calculations.

4.6 Sources of Uncertainty

4.6.1 Experiment

Estimates of the magnitudes of some of the experimental uncertainties have been given in the Chapters 2 and 3. A more complete description and summary will be given in this section.

Naturally, more sources of uncertainty are present for absolute measurements than for relative measurements. The error bars for the H(p,p) cross sections shown in Fig 3.3 contain (as well as statistical uncertainties of $\approx$.3–.5%), uncertainties in wire chamber efficiencies and electronics dead time ($\approx$.6%, combined), relative momentum acceptance ($\approx$1.5%), target thickness ($\approx$1.5%), target composition ($\approx$.3%), absolute beam-charge normalization ($\approx$.7%) and solid angle ($\approx$1%). All of the systematic uncertainties added in quadrature give a combined systematic uncertainty of 2.5%. There is also an uncertainty (of undetermined magnitude) in the absolute normalization of the momentum acceptance function. This could be checked if there was a precisely determined cross section in our energy range with which we could compare our value. Unfortunately this is not the case.

For (p,p′) cross sections measured relative to the SP88 PP phase-shift solution several of the sources of uncertainty are not included, namely wire chamber efficiencies, electronics dead time, beam-charge normalization and solid angle. The remaining quantities give a combined systematic uncertainty for the relative (p,p′) measurements of 2.1%. We note that the (p,p′) uncertainties listed in Table 3.2 and Table 3.3 are statistical only.

The systematic uncertainties for the (n,p) cross sections are the same as for the relative (p,p′) cross sections, with the addition of an uncertainty in the relative efficiencies of the target box wire planes. As this contribution is negligibly small ($\leq .1\%$) it is not considered. Again, the tabulated uncertainties are statistical only.

Because the (p,n) cross sections depend on run-to-run comparisons of target yields, the estimated variations in beam-charge normalization, wire plane efficiencies and electronics dead time ($\approx 1.8\%$ for ^{6}Li; $\approx 1.2\%$ for ^{12}C) should be included in the tabulated uncertainty, but only for the ^{6}Li(p,n) datum; the ^{12}C(p,n) datum only contains experimental information from the ^{12}C(n,p) data so the uncertainty in this case is derived from the (n,p) data. There may also be an uncertainty of several per cent in the determination of the ^{6}Li(p,n) peak area (see Fig. 3.10); there was really no sound basis for determining the area in the manner described in Chapter 3. Taking the position (for now) that the theoretical calculations for $A = 6$ are valid, the fact that the ratio of experiment to theory is greater for the (p,n) reaction than for (p,p′) is consistent with a slight over-estimate of the ^{6}Li(p,n) peak area. This can certainly not be ruled out. There is also a $J^\pi=2^+$ state in ^{6}Be at 1.67 MeV (see Fig. 1.2) which would only be partially resolvable with the current data, although it is quite plausible to expect the contribution from this state to be negligibly small at such a small angle. Examination of Fig. 3.10 does not reveal convincing evidence that this state is present with significant strength; it may be "buried" in the tail contribution described above.

Two potentially very significant sources of uncertainty in the comparisons of (n,p), (p,n) and (p,p′) cross sections are the relative magnitudes of the SP88 PP and NP cross sections, and the reliability of the ratio of (p,n) to (n,p) cross sections in the A=12 triad. Of the former, we note that the agreement between the ^{12}C(n,p) and ^{12}C(p,p′) cross sections suggests that the SP88 PP and NP phase-shift solutions

are consistent with each other to approximately the 3% level; and also that any possible discrepancy between them would affect the comparisons within the A=6 and A=12 triads in exactly the same way. Of the latter, the good agreement between our ^{12}C(p,n) datum and the data of Watson *et al* [28] imply that this assumption is a reasonable one, at least to the several per cent level. In Fig. 3.11 our datum includes the systematic uncertainties listed above for the (n,p) data.

In summary, the agreement of the ratios of the experimental (n,p) and (p,p′) cross sections to the theoretical calculations supports the argument that the observed asymmetry in $A = 6$ is not due to some systematic uncertainty or error in measurement. The agreement of the ^{12}C(p,n) "datum" (used to normalize the ^{6}Li(p,n) datum) with the measurements of Watson *et al* supports the validity of the unorthodox normalization procedure, but the ^{6}Li(p,n) peak area itself is difficult to determine and so may be of questionable accuracy.

4.6.2 Theory

It has already been mentioned that the shell model calculations used to find the OBTD's are known to be unreliable in predicting the energy levels of $A = 6$ nuclei. The restriction of the shell model to the 1p shell leads to the description of the ^{6}Li ground and 3.56 MeV excited states as

$$\begin{aligned} |1^+0\rangle &= A|(p_{3/2})^2;1^+0\rangle + B|p_{3/2}p_{1/2};1^+0\rangle + C|(p_{1/2})^2;1^+0\rangle \\ |0^+1\rangle &= D|(p_{3/2})^2;0^+1\rangle + E|(p_{1/2})^2;0^+1\rangle \end{aligned} \tag{4.39}$$

with the normalization conditions

$$A^2 + B^2 + C^2 = D^2 + E^2 = 1 \tag{4.40}$$

Several authors (e.g. [20,52]) have suggested that ^{6}Li is "somewhat of an enigma among light nuclei". The ground state charge density cannot be fit to a simple

harmonic oscillator distribution

$$\rho(r) = \rho_0 \left(1 + \alpha(r/a)^2\right) e^{\left(-(r/a)^2\right)} \tag{4.41}$$

unlike all other nuclei in its mass region. The 3^+ and 0^+ radial wave functions are inconsistent with the 1p harmonic oscillator basis [53], and require modifications to the radial wave functions in order to fit the electron scattering data. It might be argued that the method of Cohen and Kurath used to obtain the ^{6}Li wave functions would be less reliable than one in which only the properties of ^{6}Li (as opposed to the entire 1p-shell) were considered. Such a procedure was adopted by Donnelly and Walecka [54]. They required that the wave functions (in a 1p harmonic oscillator basis) fit the ground state magnetic and quadrupole moments and the transverse magnetic form factors for both elastic and inelastic scattering. These properties are (in principle) determined only by the valence nucleons. The use of a single harmonic oscillator parameter to fit both the weak and electromagnetic data implicitly assumes isospin symmetry. The parameters obtained are very similar to those of Cohen and Kurath, as is shown in Table 4.4. Weak quantities such as the ^{6}He β decay rate and the ^{6}Li μ capture rate calculated with their wave functions also agree with experimental rates.

The Donnelly-Walecka wave functions, when used with their simultaneously fit harmonic oscillator parameter of $b = 2.03$ fm, gave a reasonable fit to the small-q (p,p′) data, but like the Cohen-Kurath wave functions could not simultaneously fit the (n,p) and (p,p′) data.

There have been other attempts to fit the ^{6}Li wave functions to electromagnetic and weak properties within the context of the shell model [20,53,55] with limited degrees of success. It may be instructive to consider the validity of using harmonic oscillator wave functions to describe the nuclear structure for the A=6 system. We

	A	B	C	D	E
Cohen/Kurath	-0.564	0.821	0.089	0.83	0.56
Donnelly/Walecka	-0.581	0.810	0.084	0.80	0.60
		OBTD		$j_f j_i$	
	$\frac{1}{2}\frac{1}{2}$	$\frac{1}{2}\frac{3}{2}$	$\frac{3}{2}\frac{1}{2}$	$\frac{3}{2}\frac{3}{2}$	
Cohen/Kurath	0.029	0.187	-0.197	0.191	
Donnelly/Walecka	0.029	0.142	-0.134	0.2644	

Table 4.4: Comparison of shell model wave functions of Cohen and Kurath [31] and Donnelly and Walecka [54]. The lower part compares the one-body transition densities.

note that Bergstrom *et al* [20,55] conclude that pure 1p-shell harmonic oscillator wave functions do not describe the ^{6}Li M1 transverse magnetic form factor very well, particularly at large momentum transfers. Nonetheless, they deduce a value of $b \approx 1.83$ fm, with the oscillator parameter constrained to reproduce the observed diffraction minimum at $q = 1.40$ fm^{-1}. Perroud *et al* [56], using Bergstrom's data, obtain a good fit over the entire range of momentum transfers ($\approx .25$ to 5 fm^{-1}) by introducing a linear variation into the harmonic oscillator parameter b, i.e.

$$b = b_0 + b_1 q \tag{4.42}$$

While they admit no physical justification for this procedure, the values they obtain ($b_0 = 2.19$ fm ; $b_1 = -.24$ fm^2) give $b = 2.12$ for $q = .3$ fm , in reasonable agreement with b determined from our low-q (p,p') data. Another serious drawback to using an harmonic oscillator potential is the inability to describe unbound states, such as the ground state of ^{6}Be.

It may be that the problem lies in the use of the shell model itself. There is much evidence (such as the abnormally large RMS radius, given in Table 4.2) to suggest that the most accurate descriptions of the ^{6}Li structure will be given by cluster models. The ^{6}Li nucleus is treated as an α-d bound state. Three harmonic oscillator

parameters are now used to describe the system: the internal α-particle oscillator α; the internal deuteron parameter β; and γ, which represents the relative motion of the clusters. The shell model is obtained in the limit $\alpha = \beta = \gamma$. A relatively simple model [55] has been developed which can be made to simultaneously fit all the electromagnetic form factors when the deuteron is allowed to deform along the line joining the center of masses of the clusters. The $T = 0$ ground ($T = 1$ 3.56 MeV) state is considered to be pure $^3S_1$ ($^1S_0$). Thus the transition is considered to be entirely a spin flip of one of the nucleons. It is pointed out that although the 3.56 MeV level has a P-state amplitude of $\approx .5$, over 90% of the transition amplitude is spin flip. The equivalent representation of this picture in the shell model would be the usual closed 1s core with two valence nucleons with *different* oscillator parameters, and which mutually interact with each other with another independent oscillator parameter. This "residual" interaction is not present in the simple single-particle model.

We may also wish to re-examine our assumptions about the optical potentials. For $A = 12$ we assumed that the matter distribution had the same shape for all three final-state nuclei. This appears to have been a reasonable approximation based on the consistency of the (n,p) and (p,p') cross sections. The discrepancy between the (p,p') data and theoretical angular distribution may indicate some inaccuracy in using the ground state density to describe the 15.1 MeV density, but on the other hand could be because the Love-Franey prescription for deriving the N-nucleus effective interaction from the NN interaction does not describe the true q-dependence of the N-nucleus force.

The same argument as in the preceding paragraph could be made about the excited state optical potential for the ^{6}Li(p,p') calculation. The assumptions made about the proton (neutron) distributions in ^{6}He (^{6}Be) should be quite reasonable

because we would expect the ^{4}He core in the $A = 6$ nuclei to have essentially the same properties as a free ^{4}He nucleus. This may not be the case for the neutron (proton) distributions in ^{6}He (^{6}Be), which were derived from the charge density of ^{9}Be. The shape and radius of the distribution depend not only on the number of protons, but also on the number of neutron-proton pairs in the nucleus. The alternative would have been to retain the same shape parameters as for ^{6}Li as was done for ^{12}C.

Finally, we look at the Love-Franey effective interaction. The agreement of the *shape* of the SP88 PP phase shift solution with the angular distribution of the H(p,p) data would apparently indicate that the q-dependence of the effective NN interaction is quite good in this energy range. But as was suggested above, it is probably reasonable to question the validity of the Love-Franey prescription for the transformation to the N-nucleus situation. This is apparent in the very large overall normalizations that must be applied to make the calculations agree with the data, even for a nucleus like ^{12}C whose structure is considered to be very well known.

Chapter 5

Summary and Conclusions

The original aim of this experiment was to determine the $\vec{\sigma}\vec{\tau}$ nuclear matrix element for populating the 3.56 MeV $J^{\pi}=0^{+};T = 1$ state in ^{6}Li. If accurately determined, comparison of this matrix element with the M1 matrix element determined from the γ decay width measured in (e,e') scattering could measure orbital effects and meson exchange currents which contribute significantly to the M1 matrix element but not to the $\vec{\sigma}\vec{\tau}$ matrix element. These effects can be reliably calculated for ^{6}Li, and any remaining discrepancy between the M1 and $\vec{\sigma}\vec{\tau}$ matrix elements after subtracting them could be attributed to a renormalization of the nuclear magnetic moment inside the nucleus. In the cloudy bag quark model such a renormalization can be attributed to a swelling of the nucleon inside the nucleus because in that model the magnetic moment of the "bag" scales with its radius. This calculation has been done for ^{12}C, with an upper limit for the rescaling of the nucleon magnetic moment placed at 2%.

The well-known proportionality of 0°, $q = 0$ (n,p) reaction cross sections to Gamow-Teller β decay strength allows the calibration of the proportionality constant to be obtained by comparing the known ft value for ^{6}He β decay to the ^{6}Li(n,p)^{6}He reaction cross section. The ^{6}Li(p,n)^{6}Be cross section is also required to determine if there is any possible isospin symmetry breaking in the multiplet.

Isospin symmetry breaking may be expected between the three reactions due to differences in binding energies in the final-state nuclei. The extraction of the matrix element depends on being able to accurately model the reactions in order that the extrapolation to the $q = 0$ cross section be reliable.

Because the nuclear structure of ^{12}C is well known, and because the observed β decay ft asymmetry has already been shown to be due to binding energy differences the same set of measurements was performed on ^{12}C. The proportionality described above implies an asymmetry of the same magnitude as the observed ft asymmetry should manifest itself in the cross section measurements, and in the theoretical calculations if the binding energy differences are accounted for in the model. These measurements acted as a control on the experimental method and analysis, and also on the theoretical calculations where they had to demonstrate whether or not cross section ratios for the different reactions could be calculated to an accuracy of several per cent.

We have measured (n,p), (p,n) and (p,p') reaction cross sections for ^{12}C and ^{6}Li targets to A=12 and A=6 isospin multiplets. Realistic DWIA calculations give values for the ft asymmetry and ratios of (n,p) to (p,p') cross sections for A=12 in good agreement with data. The calculated ratio of (n,p) to (p,n) cross sections is the same size ($\approx$ 13%) as the observed ft asymmetry. As well as confirming the proportionality of GT β decay strength to forward angle nucleon-nucleus cross sections, this result also confirms that observed asymmetries in reaction cross sections to members of an isospin multiplet are due to binding energy differences, as is the case for ft asymmetries in β decay.

Similar calculations for the A=6 system which assume that isospin symmetry is conserved show a discrepancy of $\approx$ 5% between (n,p) and (p,n) cross sections, compared with (p,p') cross sections taken at finite q values; this asymmetry may become

neglible upon extrapolation to $q = 0$. The experimental angular distributions for ^{6}Li(p,p′) and ^{6}Li(n,p) reactions show differences *versus* q which are not reproduced by the theoretical calculations. Comparison with DWIA model predictions shows a discrepancy of up to 45% at $q = 0.65$ fm^{-1}. This discrepancy warrants further investigation, both experimentally and theoretically: in the former case it would be very useful to measure the corresponding angular distribution for the ^{6}Li(p,n)^{6}Be reaction to see if it displays similar tendencies as the (n,p) reaction; in the latter case some modification to the model is required to reporduce differences of such a large magnitude. This reflects our uncertainty in the reaction models (t_{NA}; optical potentials) and the nuclear structure (transition densities; matter distributions in the multiplet). The inability to accurately model the reactions for $A = 6$ makes any reliable estimates or conclusions about the $\vec{\sigma}\vec{\tau}$ matrix element for the ^{6}Li(p,p′) reaction difficult unless progress can be made in understanding the q-dependence of the (p,p′) and (n,p) data.

A better theoretical description of the nuclear structures of the lower p-shell nuclei would seem to be a necessary ingredient for a better understanding of the various effects which may be present. In particular it appears that it is necessary to somehow include the efects of α-d clustering in any description of the nuclear structure for $A = 6$, or in the context of the shell model to expand the model space beyond the 1p shell.

The method used to normalize the ^{6}Li(p,n)^{6}Be reaction, which relies on the ratio of (n,p) to (p,n) cross sections from a DWIA calculation, gives a value of the ^{12}C(p,n)^{12}N(g.s.) cross section consistent with the absolute cross sections measured by Watson *et al.* This normalization scheme gives consistency between the (p,n), (n,p) and (p,p′) reaction cross sections relative to the SP88 phase shift solution.

As a byproduct, absolute H(p,p) cross sections have been measured at 280 MeV

over a range of $\theta_{c.m.} = 8$–$23°$. The shape of the angular distribution agrees very well with the SP88 PP phase shift solution, but the experimental cross sections, while agreeing with other data taken at 285 MeV, are lower than SP88 by $\approx 7.5\%$. We believe this discrepancy to be real; however, the general difficulties in measuring absolute cross sections, and the lack of precise NN cross sections in this energy region make it hazardous to be completely confident about this. Discrepancies between SP88 and data at many other energies in the range of 100–500 MeV (for both (p,p) and (n,p) scattering) indicate that a set of accurate and consistent NN cross section measurements at medium energies are required in order to make reliable comparisons between (n,p) and (p,p′) cross sections such as were necessary for this experiment.

References

[1] W. Heisenberg, Z. Phys. **77**, 1 (1932).

[2] H. Yukawa, Proc. Phys. Math. Soc. Japan **17**, 48 (1935).

[3] R.D. Present, Phys. Rev. **50**, 635 (1936).

[4] M.A. Tuve, N.P. Heydenburg and L.R. Hafstad, Phys. Rev. **50**, 806 (1936).

[5] G. Breit, E.U. Condon and R.D. Present, Phys. Rev. **50**, 825 (1936).

[6] G. Breit and E. Feenberg, Phys. Rev. **50**, 850 (1936).

[7] L.A. Young, Phys. Rev. **47**, 972 (1935).

[8] E.P. Wigner, Phys. Rev. **51**, 106 (1937).

[9] N. Kemmer, Proc. Camb. Phil. Soc. **34**, 354 (1938).

[10] M.J. Moravcsik, Phys. Rev. **136**, B624 (1964).

[11] I. Šlaus, Y. Yoshinori and H. Tanaka, Phys. Rep. **173**, 257 (1989).

[12] K.K. Seth, in *Weak and Electromagnetic Interactions in Nuclei*, proceedings of the International Symposium, Heidelberg, edited by H.V. Klapdor (Springer-Verlag, Heidelberg, 1986).

[13] H. Sato, Nucl. Phys. **A269**, 378 (1976).

[14] N. Auerbach, Phys. Rep. **98**, 273 (1983).

[15] F. Ajzenberg-Selove, Nucl. Phys. **A413**, 1 (1984).

[16] D.H. Wilkinson and D.E. Alburger, Phys. Rev. Lett. **26** 1127 (1971).

[17] J. Blomqvist, Phys. Lett. **B35**, 375 (1971).

[18] I.S. Towner and J.C.Hardy, in *Proceedings of the 7th International Conference on Atomic Masses and Fundamental Constants*, edited by O. Klepper (Technische Hochschule Darmstadt Lehrdruckerei, Darmstadt, 1984).

[19] T.N. Taddeucci, C.A. Goulding, T.A. Carey, R.C. Byrd, C.D. Goodman, C. Gaarde, J. Larsen, D. Horen, J. Rapaport, and E. Sugarbaker, Nucl. Phys. **A469**, 125 (1987).

[20] J.C. Bergstrom, U. Deutschmann, and R. Neuhausen, Nucl. Phys. **A327**, 439 (1979).

[21] P.A.M. Guichon and C. Samour, Nucl. Phys. **A382**, 461 (1982).

[22] P. Blunden, private communication.

[23] M.A. Morgan, G.A. Miller and A.W. Thomas, Phys. Rev. **D33**, 817 (1986).

[24] T.E.O. Ericson and A. Richter, Phys. Lett. **B184**, 249 (1987).

[25] D.H. Wilkinson, Nucl. Phys. **A377**, 474 (1982).

[26] Computer code DW81, Arizona State University, J.R. Comfort.

[27] F. Ajzenberg-Selove, Nucl. Phys. **A490**, 1 (1988).

[28] J.W. Watson *et al*, Phys. Rev. **C40**, 22 (1989).

[29] J. D'Auria, M. Dombsky, L. Moritz, T. Ruth, G. Sheffer, T.E. Ward, C.C. Foster, J.W. Watson, B.D. Anderson, and J. Rapaport, Phys. Rev. **C30**, 1999 (1984).

[30] R.A. Arndt and L.D. Roper, Scattering Analysis Interactive Dial-in (SAID) program, unpublished.

[31] S. Cohen and D. Kurath, Nucl. Phys. **73**, 1 (1965).

[32] MRS Manual, TRIUMF, unpublished.

[33] R. Helmer, Can. J. Phys. **65**, 588 (1987).

[34] R. Abegg and R. Schubank, TRIUMF Report No. TRI-DN-87-17, 1987 (unpublished).

[35] R.S. Henderson, K.H. Hicks, C.A. Miller, M.C. Vetterli, O. Häusser, W.P. Alford, K.P. Jackson, S. Yen, and D. Frekers, Nucl. Inst. and Methods **A257**, 97 (1987).

[36] D. Aebischer *et al*, Phys. Rev. **D13**, 2478 (1976).

[37] W.G. Love and M.A. Franey, Phys. Rev. **C24**, 1073 (1981).

[38] M.A. Franey and W.G. Love, Phys. Rev. **C31**, 488 (1985).

[39] B.A. Brown, A. Etchegoyen and W.D.M. Rae, **OXBASH: The Oxford-Buenos-Aires-MSU Shell-Model Code**, unpublished, (1985).

[40] J.B. Flanz, R.S. Hicks, R.A. Lindgren, G.A. Peterson, J. Dubach and W.C. Haxton, Phys. Rev. Lett. **43**, 1922 (1979).

[41] R.A. Arndt *et al*, Phys. Rev. **D28**, 97 (1983).

[42] K. Merle, in *Proceedings of the International Conference on Photonuclear Reactions and Applications*, Asilomar (California), 1973, edited by B.L. Berman (NTIS, Springfield, Virginia, 1973).

[43] G.C. Li, I. Sick, R.R. Whitney and M.R. Yearian, Nucl. Phys. **A162**, 583 (1971).

[44] J.S. McCarthy, I. Sick, R.R. Whitney and M.R. Yearian, cited in C.W. de Jager, H. de Vries and C. de Vries, Atomic Data and Nuclear Data Tables **14**, 479 (1974).

[45] J.A. Jansen, R.Th. Peerdeman and C. de Vries, Nucl. Phys. **A188**, 337 (1972).

[46] MAINX8 Microscopic Optical Potential Program, unpublished.

[47] A. Johansson, U. Svandberg and O. Sundberg, Arkiv Fysik **19**, 527 (1961).

[48] G.P. Millburn, W. Birnbaum, W.E. Crandall and L. Schecter, Phys. Rev. **95**, 1268 (1954).

[49] L.R.B. Elton and A. Swift, Nucl. Phys. **A94**, 52 (1967).

[50] K.P. Jackson *et al*, Phys. Lett. **B201**, 25 (1988).

[51] A. Celler, private communication (1990).

[52] C.W. Glover *et al*, preprint (1986).

[53] J.C. Bergstrom, I.P. Auer and R.S. Hicks, Nucl. Phys. **A251**, 401 (1975).

[54] T.W. Donnelly and J.D. Walecka, Phys. Lett. **44B**, 330 (1973).

[55] J.C. Bergstrom, S.B. Kowalski, and R. Neuhausen, Phys. Rev. **C25**, 1156 (1982).

[56] J.P. Perroud, A. Perrenoud, J.C. Alder, B. Gabioud, C. Joseph, J.F. Loude, N. Morel, M.T. Tran, E. Winklemann, H. von Fellenberg, G. Strassner, P. Truöl, W. Dahme, H. Panke, and D. Renker, Nucl. Phys. **A453**, 542 (1986).